doi: 10.82124/CEAS-GNC-2026-080 CEAS-GNC-2026-080

Improved Longitudinal Stall Modeling with Separable Nonlinear Least Squares and Dynamic Stall Maneuvers

Joey A. Herbold MSc Student, Department of Control & Simulation, Faculty of Aerospace Engineering, Delft University of Technology, Delft, Netherlands. joey@herbold.nl

Daan M. Pool Assistant Professor, Department of Control & Simulation, Faculty of Aerospace Engineering, Delft, Netherlands. D.M.Pool@tudelft.nl

Coen C. de Visser Associate Professor, Department of Control & Simulation, Faculty of Aerospace Engineering, Delft, Netherlands. C.C.deVisser@tudelft.nl

ABSTRACT

Loss of control inflight is the most common cause of fatal accidents in aviation. Aerodynamic stall models are utilized in pilot training to enhance safety and prevent accidents. This research presents an advanced longitudinal stall model for the Cessna Citation II, achieved through innovations in modeling methodologies and experimental design. By introducing dynamic stall maneuvers with step inputs, the study mitigated τ_1 and τ_2 parameter correlation, enabling more reliable parameter identification. A separable nonlinear least squares method significantly reduced computational time for nonlinear stall model estimation, decreasing it from hours to seconds. This approach revealed two minimally correlated flow separation states, offering deeper insights into wing flow characteristics and improving model accuracy. The lift model was refined to incorporate pitch rate and elevator deflection effects, while the drag model was enhanced with a lift-induced drag component. Additionally, a center of pressure model was derived from pitching moment data, advancing the understanding of stability during stall. A novel structure for characterizing degraded elevator control effectiveness was also developed. These advancements resulted in substantial performance improvements, with mean squared errors for lift, drag, and pitch moment coefficients reduced by 32%, 29%, and 27%, respectively. The models also demonstrated greater consistency across diverse maneuvers, evidenced by reduced variability in R^2 values. This work contributes to more accurate stall modeling, enhancing both aerodynamic understanding and aviation safety.

Keywords: SNLS, Separable Nonlinear Least Squares, Stall modeling, Dynamic stall, Kirchhoff separation model, Longitudinal dynamics, Cessna Citation

Nomenclature

Roman Symbols

FL	=	Flight level
LOC-I	=	Loss of control in-flight
MSE	=	Mean square error
OLS	=	Ordinary least squares

SNLS	=	Separable nonlinear least squares
UPRT	=	Upset prevention and recovery training
a_x,a_y,a_z	=	Accelerations in F_b [m/s^2]
a_1	=	Stall abruptness parameter [-]
b	=	Wing span [m]
$\bar{c}$	=	Mean aerodynamic chord [m]
$\boldsymbol{c}$	=	Linear parameters
C_D	=	Drag coefficient [-]
C_L	=	Lift coefficient [-]
C_m	=	Pitch moment coefficient [-]
C_N	=	Normal force coefficient for an airfoil [-]
C_T	=	Thrust coefficient [-]
C_X	=	Longitudinal force coefficient [-]
C_Z	=	Normal force coefficient for an aircraft [-]
$D*$	=	Fréchet derivative of $*$
F_*	=	Reference frame
I_*	=	Moment of inertia around $*$ axis [kgm^2]
$\boldsymbol{I}$	=	Inertia tensor [kgm^2]
K	=	Coefficient relating the pitch moment
	=	coefficient to the lift coefficient
$\boldsymbol{L}$	=	Loss function
m	=	Mass [kg]
p,q,r	=	Roll, pitch and yaw rate in F_b [rad/s]
$\boldsymbol{P}^{\perp}_{\boldsymbol{\Phi}(\boldsymbol{\theta})}$	=	Projector onto the orthogonal complement of the column space of $\boldsymbol{\Phi}(\boldsymbol{\theta})$
$\bar{q}$	=	Dynamic pressure [Pa]
$\boldsymbol{r}$	=	Residual vector
R^2	=	Coefficient of determination
$\mathbb{R}$	=	Set of real numbers
S	=	Wing surface area [m^2]
X	=	Separation state [-]
$\boldsymbol{X}$	=	Regression matrix for linear model
x,y,z	=	Coordinate in body reference frame [m]

Greek Symbols

α	=	Angle of attack [rad]
α^*	=	Stall angle of attack [rad]
β	=	Angle of sideslip [rad]
δ_a,δ_e,δ_r	=	Aileron, elevator and rudder deflection [rad]
$\boldsymbol{\theta}$	=	Nonlinear parameters
τ_1	=	Flow relaxation time constant [s]
τ_2	=	Delay of flow separation time constant [s]
$\boldsymbol{\Phi}$	=	Regression matrix for nonlinear model

Subscripts

0	=	Static relation

$_0$ = Bias term
$_a$ = Aerodynamic reference frame
$_b$ = Body reference frame
$_{c.g.}$ = Center of gravity
$_{c.p.}$ = Center of pressure
$_E$ = Earth reference frame
$_{ss}$ = Stall Strip
$_T$ = Thrust
$_w$ = Remainder of the wing

Superscripts

$\hat{}$ = Model prediction
$\hat{}$ = Optimal parameter estimate
$\dot{}$ = Time derivative
$^+$ = Moore-Penrose pseudo inverse

1 Introduction

Loss of control in-flight (LOC-I) remains a critical safety concern in aviation, responsible for a majority of fatal accidents over the past decades [1–4]. LOC-I occurs when a pilot is unable to maintain control and the aircraft deviates from its intended flight path. Stalls have been shown to be a common precursor to LOC-I incidents [5, 6]. In a study of 74 LOC-I accidents between 1993 and 2007, 36% were caused by aerodynamic stall [7]. If not correctly recognized, a stall can escalate into a more severe upset. Therefore, pilots' recognition of stalls is seen as a fundamental aspect of accident prevention [8]. The critical nature of stall recognition in LOC-I scenarios underscores the importance of effective upset prevention and recovery training (UPRT). Training goals have been put forward by the International Committee for Aviation Training in Extended Envelopes (ICATEE) [9] and are currently adopted by ICAO, FAA, and EASA [10–12]. Analysis of training goals showed that it is necessary to improve the aerodynamic models in stall regimes for flight simulator training devices [13].

There are two methods for the determination of stall models. The first is based on extensive wind tunnel testing and CFD analysis, for example, the simulation of upset recovery in aviation (SUPRA) project [14]. These projects are expensive due to the high complexity and extensive use of wind tunnels. Moreover, scaling effects complicate the interpretation of results. Alternatively, identification methods are used on flight test data. Stall model identification has been extensively researched at different research institutes and universities, such as the German Aerospace Center (DLR) [15–18], NASA [19], the Flight Test and Research Institute of the Brazilian Air Force [20, 21], and TU Delft [22–29].

Stall models generally combine differential equations to model flow separation with polynomial linear-in-the-parameters model structures to determine the aerodynamic forces resulting in a nonlinear optimization problem. This problem was previously solved in a multi-stage approach [30], which has been proven to be computationally expensive and often leads to local optima. The main contribution of this work is a novel model parameter estimation methodology that combines separable nonlinear least squares (SNLS) with Kirchhoff's theory of flow separation, allowing for more complex model structures that still converge to an optimal solution. Separable nonlinear least squares (SNLS) implicitly calculates the ordinary least squares (OLS) estimate for the linear parameters, which reduces the dimension of the nonlinear parameter space [31]. This is shown to improve the convergence rate [32].

The new parameter estimation technique is applied to the identification of a longitudinal dynamics model for the TU Delft's Cessna Citation II research aircraft. New flight tests have been performed for the new longitudinal model. The dynamic stall and deep dynamic stall aim to reduce the correlation between τ_1 and τ_2 which was found to be high with a new correlation calculation. Improvements are proposed to include local flow effects of the stall strips installed on the wing. Furthermore, elevator and pitch rate effects are incorporated into the model. A new approach involving the lift-induced drag is introduced for the drag model. The pitch model is upgraded by including a model for the shift in the center of pressure at high angles of attack. Lastly, a new model for elevator control effectiveness is identified.

This paper is organized as follows: Section 2 provides an overview of the prerequisites required for the rest of the paper. Next, the developed methodology for this work is presented in Section 3. This is followed by Section 4, which presents the results. A discussion is performed in Section 5 and finally, Section 6 concludes the paper.

2 Background

2.1 Flight Test Vehicle

The Cessna Citation II callsign PH-LAB, is a research aircraft operated by Delft University of Technology. The aircraft is jointly owned by the University and the Netherlands Aerospace Center. The aircraft is used for educational and research purposes and offers a unique opportunity for stall model identification. Its general dimensions are presented in Table 1. Figure 1 shows a schematic view of the aircraft. The aircraft is outfitted with a custom flight test instrumentation system that logs aircraft states, a summary of the relevant sensed states is given in Table 2.

Table 1 General dimensions of the Cessna Citation II and mass and inertia properties at basic empty weight.

Dimensions	Value	Unit
b	15.75	m
$\bar{c}$	2.013	m
S	30.0	m^2
m	4161.3	kg
I_{xx}	12392	kgm^2
I_{yy}	31501	kgm^2
I_{zz}	41908	kgm^2
I_{xz}	2252.2	kgm^2

Note that values differ slightly from Van Ingen et al. [30] as they are derived directly from the manufacturer's manual

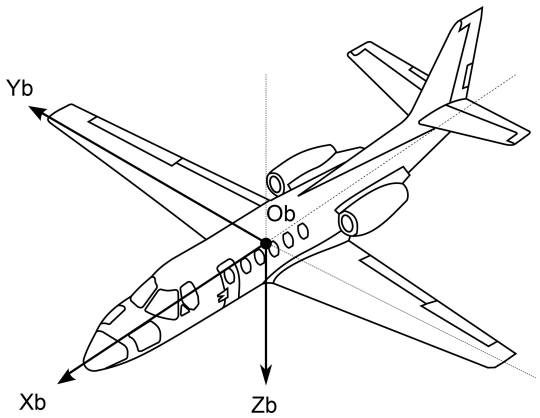

Fig. 1 Schematic view of the Cessna Citation II. Adapted from [30].

2.2 Aerodynamic Coefficients

Aerodynamic coefficients express the aerodynamic forces and moments on the aircraft. These coefficients are dimensionless versions of the forces and moments themselves. In the body reference

Table 2 Summary of the relevant sensing systems of the flight test instrumentation system.

System	Explanation	Measures	Variables	Unit	Sample rate
AHRS	Attitude & Heading Reference System	Aircraft Attitude	φ, θ, ψ	rad	52 Hz
		Body Rotation Rates	p, q, r	rad/s	
		Body Specific Forces	S_x, S_y, S_z	m/s^2	
Boom	Air Data Boom	Air Incidence Angles	α, β	rad	100 Hz
DADC	Digital Air Data Computer	True Airspeed	V_{TAS}	m/s	16 Hz
		Dynamic Pressure	$\bar{q}$	Pa	8 Hz
Engine	Engine Measurements	Rotational Rates	N_1, N_2	%	1000 Hz
		Fuel Mass Flow	$\dot{m}_f$	kg/s	
GPS	Global Positioning System	Position in F_E	x_E, y_E, z_E	m	1 Hz
		Velocity in F_E	$\dot{x}_E, \dot{y}_E, \dot{z}_E$	m/s	
Synchro	Angle Measurements	Control Surface Deflections	$\delta_a, \delta_e, \delta_r$	rad	100 Hz

frame (see Appendix A), forces along X_b, Y_b and Z_b, can be defined as X^b, Y^b and Z^b respectively.

$$C_{X^b} = \frac{X^b}{\bar{q}S}, \quad C_{Y^b} = \frac{Y^b}{\bar{q}S}, \quad C_{Z^b} = \frac{Z^b}{\bar{q}S} \tag{1}$$

Equation (1) shows the non-dimensional forces in the body reference frame. In these equations, $\bar{q}$ refers to the dynamic pressure and S is the surface area of the wing.

$$C_l = \frac{L}{\bar{q}Sb}, \quad C_m = \frac{M}{\bar{q}S\bar{c}}, \quad C_n = \frac{N}{\bar{q}Sb} \tag{2}$$

Equation (2) shows the non-dimensional moments in the body reference frame. Here, b refers to the wingspan and $\bar{c}$ to the mean aerodynamic chord. Furthermore, the moments are defined as L, M, N around the axes X_b, Y_b and Z_b, respectively.

In the literature, it is also common to find the forces expressed in the aerodynamic reference frame (see Appendix A). The relationship between the reference frames is the rotation matrix $\mathbb{T}_{ab}$ (see Appendix A), which can convert the forces and moments in the body frame to those of the aerodynamic frame. The forces X^a and Z^a in the aerodynamic reference frame relate directly to the lift $L = -Z^a$ and the drag $D = -X^a$ of the aircraft.

Aerodynamic forces and moments cannot be measured directly in the aircraft. Instead, they are derived from the specific force and body rate data provided by the AHRS. The accelerations a_x, a_y, and a_z are derived from the specific force [23]. Acceleration is related to the sum of all forces on the vehicle. The gravitation and engine effects can be subtracted to isolate the aerodynamic force.

$$\begin{bmatrix} C_{X^b} \\ C_{Y^b} \\ C_{Z^b} \end{bmatrix} = \frac{1}{\bar{q}S} \left\{ m \begin{bmatrix} a_x^b \\ a_y^b \\ a_z^b \end{bmatrix} - m\mathbb{T}_{bE} \begin{bmatrix} 0 \\ 0 \\ g_0 \end{bmatrix} - \begin{bmatrix} X_T^b \\ Y_T^b \\ Z_T^b \end{bmatrix} \right\} \tag{3}$$

Equation (3) shows the force coefficients in the body frame. Here, m is the aircraft mass, which is time-varying and modeled by a mass model [33]. For the gravitational force, the assumption is made that the gravitational pull is constant regardless of altitude or geographical location. Furthermore, $\mathbb{T}_{bE}$ (see

Appendix A) is a rotation matrix from the earth frame (see Appendix A) to the body frame. The thrust is defined in the body frame and calculated using an engine model provided by the manufacturer [33]. This model uses the Mach number M and the low-pressure turbine speed N_1 to calculate the thrust.

The aerodynamic moment coefficients can also be derived from the equations of motion. Here, the inertial and gyroscopic moments are taken into account. Furthermore, the moment caused by the thrust of the engines can be subtracted. Lastly, the equation can be non-dimensionalized.

$$\begin{bmatrix} C_l \\ C_m \\ C_n \end{bmatrix} = \frac{1}{\bar{q}S} \begin{bmatrix} 1/b & 0 & 0 \\ 0 & 1/\bar{c} & 0 \\ 0 & 0 & 1/b \end{bmatrix} \cdot \left\{ \boldsymbol{I} \cdot \begin{bmatrix} \dot{p} \\ \dot{q} \\ \dot{r} \end{bmatrix} + \begin{bmatrix} p \\ q \\ r \end{bmatrix} \times \boldsymbol{I} \cdot \begin{bmatrix} p \\ q \\ r \end{bmatrix} - \begin{bmatrix} x_{engine} - x_{cg} \\ y_{engine} - y_{cg} \\ z_{engine} - z_{cg} \end{bmatrix} \times \begin{bmatrix} X_T^b \\ Y_T^b \\ Z_T^b \end{bmatrix} \right\} \quad (4)$$

Equation (4) shows the aerodynamic moment coefficients in the body frame. Here, p, q, and r are the roll, pitch, and yaw rates respectively. Their time derivatives are $\dot{p}$, $\dot{q}$, $\dot{r}$. The moments of inertia of the aircraft are stored in matrix $\boldsymbol{I}$, which is time-varying and modeled by the mass model [33]. The moment caused by the engine thrust uses the engine model, engine positions, and time-varying center of gravity modeled by the mass model.

2.3 Theory of Flow Separation

To link the aircraft state to the aerodynamic forces and moments at high angles of attack an intermediary is required. Additional states, in the form of flow separation states, are included to model the changing behavior at high angles of attack. First, a connection between the angle of attack and state of flow separation is established in Section 2.3.1. Then, the new flow separation state is connected to the forces and moments in Section 2.3.2.

2.3.1 Flow Separation Models

The most prominent model in aircraft stall modeling is based on Kirchhoff's theory of flow separation. This model, introduced by Goman and Khrabrov [34], connects the degree of flow separation (X) and aerodynamic forces and moments. The degree of flow separation is measured as the normalized chordwise distance at which the flow separates, $X = 1$ for attached flow and $X = 0$ for separated flow. Goman and Khrabrov noted that unsteady aerodynamic effects can cause relaxation and delay of flow separation. The following first-order differential equation can model these effects:

$$\tau_1 \frac{dX}{dt} + X = X_0(\alpha - \tau_2 \dot{\alpha}) \quad (5)$$

Here, τ_1 and τ_2 are time constants modeling relaxation and delay of flow separation, respectively. The static relationship between flow separation and angle of attack is modeled by X_0. This relation can be estimated from static wind tunnel data or identified from flight data if a model structure is assumed. Multiple model structures have been proposed [35, 36], however, in this work the model structure introduced by Fischenberg [15] is used:

$$X_0(\alpha) = \frac{1}{2} \left\{ 1 - \tanh\left(a_1 \left(\alpha - \alpha^* \right) \right) \right\} \quad (6)$$

where a_1 models the abruptness of the stall and α^* is the angle of attack at which flow separation reaches the mid chord. Using this information, three different flow separation models can be defined. Firstly, a steady flow separation model can be defined, where none of the previously mentioned unsteady effects are modeled, in other words, $\tau_1 = \tau_2 = 0$. Next, a quasi-steady model, for which τ_2 can be non-zero and

delay of flow separation is modeled. Lastly, the full unsteady model for which τ_1 and τ_2 can be non-zero. These three model structures and corresponding model parameters are summarized in Table 3.

Table 3 Different flow separation models and their corresponding model parameters.

Separation model	Parameters
Steady	a_1, α^*
Quasi-steady	τ_2, a_1, α^*
Unsteady	τ_1, τ_2, a_1, α^*

2.3.2 Force and Moment Reconstructions

Reconstructions of the aerodynamic forces and moments can be made using the state of flow separation. Initial research efforts focused on the forces and moments on airfoils. Woods [37] mentions the lift coefficient for trailing edge flow separation as:

$$C_L = 2\pi \left(\frac{1 + \sqrt{X}}{2} \right)^2 \alpha \tag{7}$$

Here, 2π is the lift curve slope in thin airfoil theory [38, p. 352] and α the angle of attack. This relation is widely accepted in aircraft stall modeling [18, 30, 34]. Next to the lift coefficient, Woods [37] defines an expression for the drag coefficient:

$$C_D = 2\pi \left(\frac{1 - \sqrt{X}}{2} \right)^2 \alpha^2 \tag{8}$$

Moving on, Leishman and Beddoes [35] have created a relation between the pitch moment coefficient C_m and the normal force coefficient C_N. In the context of aircraft, K_0 models the distance between the center of gravity and the aerodynamic center of the wing, K_1 models the shift in the center of pressure due to flow separation, and K_2 is used to describe the typical moment break of the stall. Note that a zero-lift moment C_{m_0} may be added to the model.

$$C_m = \left[K_0 + K_1(1 - X) + K_2 \sin(\pi X^m) \right] C_N \ (+C_{m_0}) \tag{9}$$

Other formulations for the pitching moment also exist. Singh and Jategaonkar [16] propose a very similar term but uses the lift coefficient instead of the normal force coefficient. Additionally, the K_0 term is neglected.

$$C_m = C_L \left[K_1(1 - X) + K_2 \sin(\pi X^m) \right] \tag{10}$$

It is not the only term for the pitching moment coefficient put forward by Singh and Jategaonkar [16]. An alternative formulation is derived from Goman and Khrabrov [34], who propose the following:

$$C_m = \frac{\pi}{2} \alpha \left(1 + \sqrt{X} \right)^2 \frac{5 \left(1 - \sqrt{X} \right)^2 + 4\sqrt{X}}{16} \tag{11}$$

This formula was then adapted by Singh and Jategaonkar [16]. They add a constant term $\frac{1}{4}$ to multiply the lift coefficient by.

$$C_m = C_L \left(\frac{5\left(1 - \sqrt{X}\right)^2 + 4\sqrt{X}}{16} - \frac{1}{4} \right) \tag{12}$$

The models and model terms introduced in this section will be used later in the paper to explore different model structures.

3 Methodology

Over the past ten years, a stall model identification workflow has been developed at Delft University of Technology. A high-level overview is visualized in Fig. 2. As can be seen, the workflow can be broken down into five major steps. First, data must be collected through flight test experiments. This is done with the Citation PH-LAB. The design of flight test experiments will be discussed in Section 3.1. Using the data collected in flight, a spectral analysis can be performed to analyze the buffet vibrations. The buffet model is created by fitting a curve to the power spectra of the normal and lateral accelerations [39]. Using the results of the buffet analysis, the buffet effects can be filtered out and flight path reconstruction can be performed, see Section 3.2.

Phases 4 and 5 are the main subject of this paper. Stall model identification, phase 4 is further detailed in Fig. 3. As can be seen in the diagram, first a model structure is assumed. The selection of the best model structure is discussed in Section 3.3. Using the assumed model structure of the lift coefficient and flow separation states, nonlinear parameter estimation is performed with SNLS. Details of the SNLS method are discussed in Section 3.4. With the estimated flow separation models the flow separation states can be determined. This is used as an input for the linear parameter estimation for the other models C_D and C_m. Linear parameter estimation is performed using OLS and is discussed in Section 3.5. Only longitudinal force and moment coefficients are mentioned, but the workflow can be extended to include lateral dynamics. After the identification, the model must be validated using additional flight data. This is discussed in Section 4.4.

3.1 Flight Test Experiments

Using the covariance calculations from Section 3.4, the correlation between τ_1 and τ_2 was re-evaluated. With this new formulation, the correlation is determined at 0.73. This was likely missed by Van Ingen et al. [30] because τ_2 ran into the lower bound of the optimization problem. This bound masked the true correlation between τ_1 and τ_2 when calculated on the resulting samples. To mitigate the correlation, new flight tests were necessary. Two new maneuvers were designed to eliminate this correlation: the dynamic and the deep dynamic stall. These maneuvers are derived from Singh and Jategaonkar [16] and adapted to fit the Citation.

The dynamic stall maneuver, depicted in Fig. 4a, starts with a smooth positive angle of attack rate. During the approach to stall, sequential step inputs are given to the elevator, ailerons, and rudder. These events are visible in Fig. 4a at annotations 1,2, and 3, respectively. The aircraft is stabilized before the aircraft enters the stall. Oscillating elevator inputs are applied to enter and exit the stall, starting at annotation 4. This gives the most information on the transition into and out of the stall.

The deep dynamic stall maneuver follows the same initial steps, as can be seen in Fig. 4b. Starting with a smooth positive angle of attack rate and sequential step inputs, again annotated with 1,2, and 3. The elevator is held to keep the aircraft in the stall. Once the angle of attack reaches 18° to 20°, oscillating elevator inputs are given. The oscillations are seen at annotation 4 as short spikes of lower deflection.

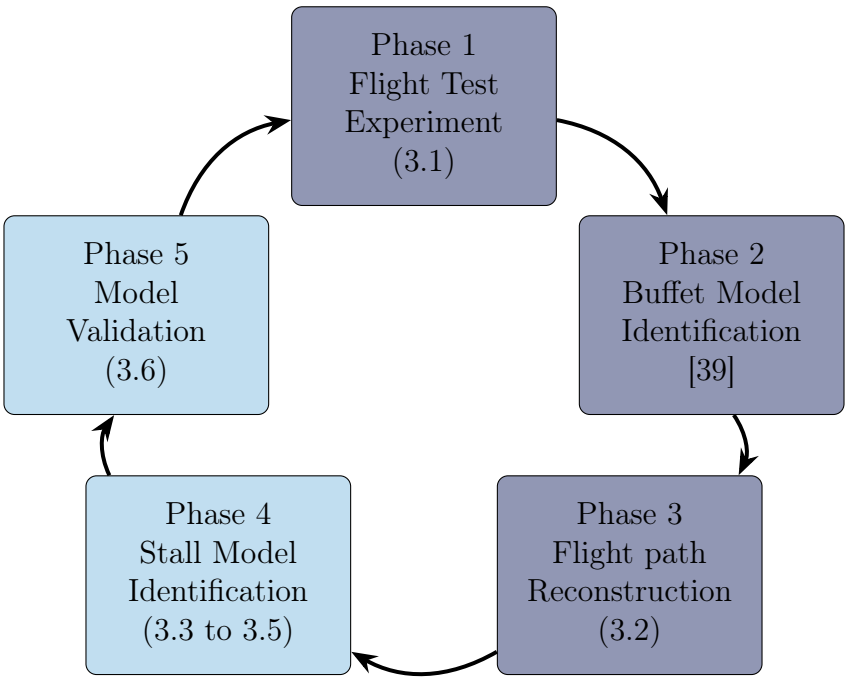

Fig. 2 System identification workflow for stall modeling. Phases four and five are the primary subjects of this research.

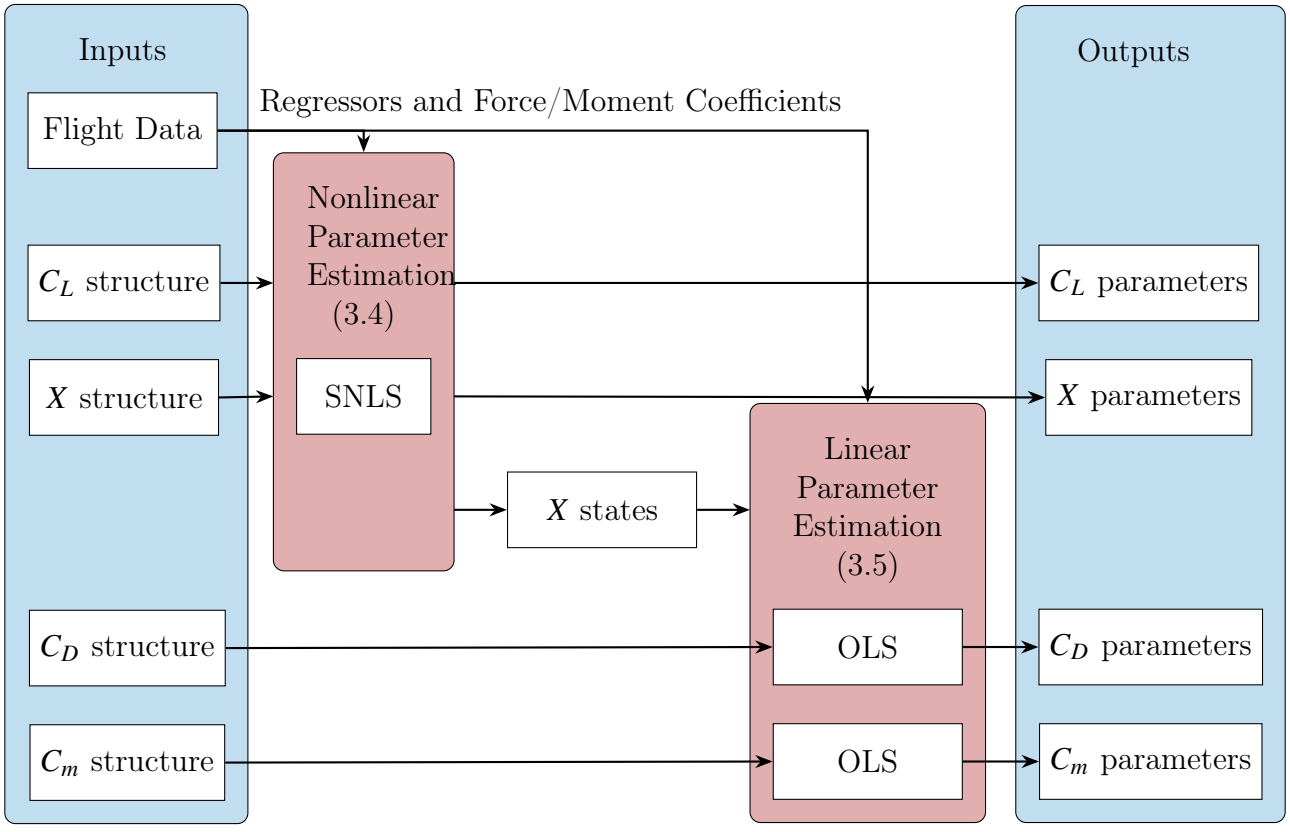

Fig. 3 Detailed description of the stall model identification workflow.

Significant elevator deflection is needed to keep the aircraft in the stall, which compromises the pilots' ability to oscillate the elevator.

Table 4 shows the data sets used in this research. First, a recap is given of the data set defined by Van Ingen et al. [30]. This prior data set is supplemented with five dynamic stalls and seven deep

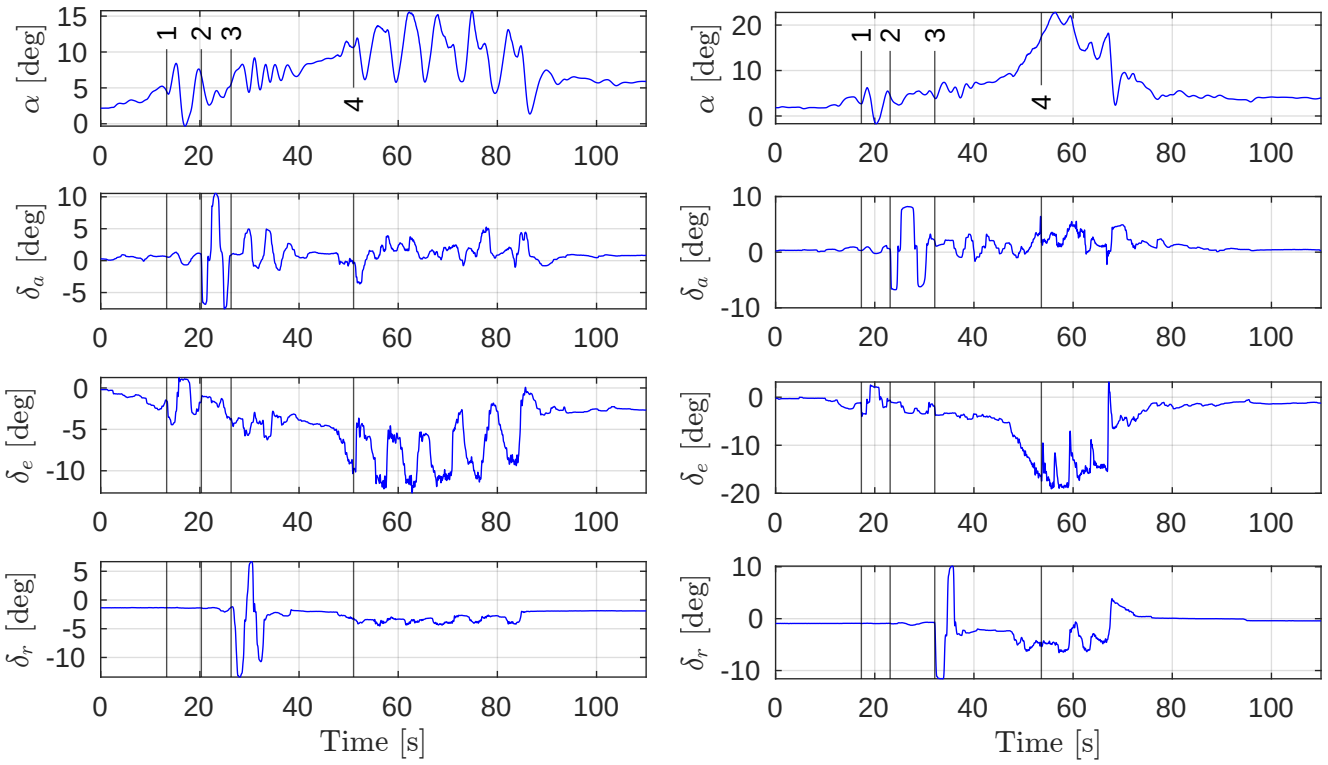

(a) Dynamic stall maneuver **(b) Deep dynamic stall maneuver**

Fig. 4 New stall maneuvers performed for this research.

dynamic stalls. These were flown between flight levels 150 and 200. The data is split into a training and validation set using an 80%-20% ratio.

Table 4 Overview of the flight maneuvers used in this paper. The division into a training and validation set is also described. The numbers in the training and validation set columns refer to the maneuver numbers.

Data set	FL	Maneuver Type	Reps	Training Set	Validation Set	Used In
Van Ingen [30]	80-110	Quasi-steady stall	2	1,2		
	110-150	Quasi-steady stall	4	3,4,6	5	4.1
	150-200	Quasi-steady stall	28	8-11,13-15,17-21,24,26-34	7,12,16,22,23,25	
This Work	80-110	Quasi-steady stall	2	1,2		
	110-150	Quasi-steady stall	4	3,4,5,6		
	150-200	Quasi-steady stall	28	8-11,13-15,17-21,24,26-34	7,12,16,22,23,25	4.2 to 4.4
	150-200	Dynamic stall	5	35-37	38,39	
	150-200	Deep dynamic stall	7	40-45	46	

3.2 Flight Path Reconstruction

Reconstructing the flight path is essential for a good identification result of aircraft systems. Sensors will introduce noise, bias, and drift, which causes errors when using the measurements directly. Kalman filtering minimizes these errors, by using a prediction model in combination with the measurements. An unscented Kalman filter is used for the state reconstruction of the Citation. The workings of this filter have been worked out in detail by Van Horssen [22] and Van Ingen [23].

Table 5 A summary of the cut-off frequencies used for the low-pass filters.

Signals	f_c [Hz]
a_x, a_y, r, δ_r	4
p, q, δ_a	5
δ_e, α, β	6
a_z	8

Some signals are strongly affected by the aerodynamic buffet, signal pre-processing must be applied to eliminate these effects [40]. This can be done using a low-pass filter. In previous research, a fourth-order Butterworth filter was used [30]. This choice is retained, although the cut-off frequencies are adjusted based on a new analysis [41]. In this analysis, the idea is to filter only as much as needed and preserve as much of the signal as possible. This is important when considering unsteady effects of unknown frequency. A summary of the new cut-off frequencies is presented in Table 5.

3.3 Model Structure

In this section, candidate models are defined to achieve specific objectives. First, the studied flow separation models are defined in Section 3.3.1. Then, the proposed lift, drag, and pitch moment models are discussed in Sections 3.3.2 to 3.3.4.

3.3.1 Separation Models

As expressed in Section 2.3, stall models typically use the state of flow separation on the wing and connect it to the aerodynamic forces and moments. This simplification stems from two-dimensional aerodynamics, however, it has proven effective for aircraft too [30]. Early-stage stall models have used one flow separation parameter for the entire aircraft [15, 30]. Later, multiple flow separation parameters were explored, but only to model asymmetric effects [17, 29]. In this work, multiple flow separation parameters are proposed for the longitudinal stall model. It is believed that previous results found by Van Ingen et al. [30] do not model a full-wing stall, but the effects of the stall strips installed on the Citation. A diagram of the stall strip can be seen in Fig. 5. The stall strip provides control of when and where the stall happens on the wing. The hypothesis would explain the low stall angle of attack found in previous work ($\alpha^* \approx 12°$) [30], which does not align with prior knowledge of the airfoils of the wing. The Citation uses NACA23014 and NACA23012 airfoils. Wind tunnel data for the NACA23012 airfoil points out that for an infinite wing at Reynolds numbers of 3.4×10^6, the stall angle of attack is at 15°. Furthermore, for a finite wing with an aspect ratio of 6, they found a stall angle of attack of 20° [42]. The Citation with an aspect ratio of 8.3 must fall somewhere in between the two.

3.3.2 Lift Model

Four goals are defined for the estimation of a new lift model. To evaluate these goals, six new models will be estimated, for which the model structures are summarized in Table 18 in Appendix B. The first goal is to evaluate the effectiveness of the new SNLS method. To make this evaluation, the model structure of Van Ingen et al. [30] is re-estimated using SNLS. This re-estimated model will be referred to as **Model CL-I**. The second goal is to evaluate if the previously used second-order spline term is necessary or an artifact of the previous nonlinear parameter estimation technique. To achieve this, the term is removed in **Model CL-II**. The third goal is to evaluate the addition of the second flow separation state, this is done through **Model CL-III**. The last goal is to re-evaluate the contributions of pitch rate q and elevator deflection δ_e. Three models are created for this. **Model CL-IV** evaluates the contribution of q. **Model CL-V** does this for δ_e and **Model CL-VI** takes into account both simultaneously.

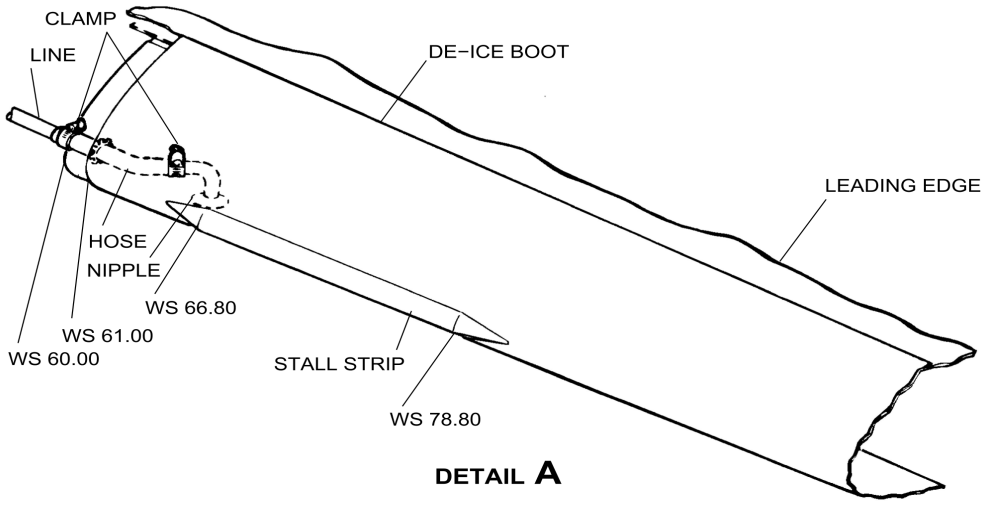

Fig. 5 Diagram of the stall strip installed on the de-ice boot on the leading edge of the wing. Adapted from the Cessna Citation II maintenance manual.

3.3.3 Drag Model

For the drag model, five objectives are set and fourteen models are defined. The model structures are summarized in Table 19 in Appendix B. As a first test, the model found by Van Ingen et al. [30] is re-estimated. This is referred to as **Model CD-I**. This re-estimation goes hand in hand with the re-estimation of **Model CL-I**. For the second objective, the same model is identified with the addition of a second flow separation term, this is **Model CD-II**. This gives an indication of the impact of the second flow separation state.

For analysis beyond the previous, it is chosen to include four terms by default: C_{D_0}, $C_{D_{q^*}}$, $C_{D_{\delta_e}}$ and $C_{D_{C_T}}$. A t-test is performed after the parameter estimation, if the hypothesis of the t-test is accepted for any parameter the model is re-estimated without the parameter. To set a baseline, the four terms are supplemented with the terms $(1 - X_{ss})$ and $(1 - X_w)$ to add stall effects. This model is referred to as **Model CD-III**.

Objective three is to analyze the relation of C_D with the angle of attack α. In previous work, a linear dependency on α was found [30]. However, it would make sense for a quadratic relation to exist, as otherwise, the drag becomes negative for negative angles of attack. For this reason, three models are suggested for comparison. The first adds a term α to the baseline and is called **Model CD-IV**. The second adds α^2 and is called **Model CD-V**. Lastly, **Model CD-VI** adds both α and α^2.

An alternative to including the angle of attack is to include the lift coefficient. Objective four is to understand the effect of including the lift coefficient as a regressor. For this, the best-performing lift coefficient model will be used as an input for the drag model. The lift coefficient model already includes stall effects. For this reason, the inclusion of C_L and C_L^2 will be tested with and without the $(1 - X_{ss})$ and $(1 - X_w)$ dependencies. This leads to six distinct models, **Model CD-VII** through **Model CD-XII**. Lastly, the drag term derived from Kirchhoff flow by Woods [37] is explored. This term also has a dependency on the state of flow separation and thus it is tested with and without the inclusion of $(1 - X_{ss})$ and $(1 - X_w)$, respectively **Model CD-XIII** and **Model CD-XIV**.

3.3.4 Pitch Moment Model

For the pitch moment model, multiple experiments are defined. First, the model by Van Ingen et al. [30] is re-estimated. This model is referred to as **Model Cm-I**. This model is identified in combination with **Model CL-I** and shows the effect of the new SNLS method.

Next, an exploration of the models proposed by Leishman and Beddoes [35] and Singh and Jategaonkar [16] is performed. Using components of their models, six base regressors are defined. First, K_0 models the moment arm between the center of gravity and the center of pressure. Then, K_1 models the shift of the center of pressure as a function of the state of flow separation. The term K_2^m is used to modify the moment to model pitch break at moment stall, here the value of m can be 1/2, 1, or 2. Lastly, K_S refers to a term proposed by Singh and Jategaonkar [16]. These six regressors are combined in fourteen ways and lead to **Model Cm-II** up to **Model Cm-XV**.

Table 6 Summary of the regressors studied in this work for the pitch moment coefficient. Note C_{m_0}, $C_{m_{C_T}}$, $C_{m_{q^*}}$ and $C_{m_{\delta_e}}$ are included by default.

Identifier	Regressors	
K_0	C_L	$x_{c.g.}/\bar{c}C_L$
K_1	$(1 - X_{ss})C_L$	$(1 - X_w)C_L$
$K_2^{1/2}$	$\sin(\pi X_{ss}^{1/2})C_L$	$\sin(\pi X_w^{1/2})C_L$
K_2^1	$\sin(\pi X_{ss}^1)C_L$	$\sin(\pi X_w^1)C_L$
K_2^2	$\sin(\pi X_{ss}^2)C_L$	$\sin(\pi X_w^2)C_L$
K_S	$\frac{5\left(1-\sqrt{X_{ss}}\right)^2+4\sqrt{X_{ss}}}{16}C_L$	$\frac{5\left(1-\sqrt{X_w}\right)^2+4\sqrt{X_w}}{16}C_L$
$(1 - X)$	$(1 - X_{ss})$	$(1 - X_w)$
$X\delta_e$	$X_{ss}\delta_e$	$X_w\delta_e$

Fischenberg and Jategaonkar [18] describe an empirical pitch moment model that includes $(1 - X)$ as a regressor. To study the inclusion of this term, **Model Cm-XVI** is defined. Furthermore, the combination of this term with previously defined regressors is studied, leading to fourteen additional model structures. These are **Model Cm-XVII** up to **Model Cm-XXX**.

The last objective is to define a new method for including stall-related elevator effectiveness reduction. To model this, a cross term of the elevator deflection δ_e and state of flow separation X_{ss} or X_w is defined. Collectively this is referred to as $X\delta_e$ but consists of two terms as can be seen in Table 6. These terms are added to the previously defined models to create 29 new models, **Model Cm-XXXI** up to **Model Cm-LXIX**. A summary of all model structures used can be found in Table 20 in Appendix B.

3.4 Nonlinear Parameter Estimation - Separable Nonlinear Least Squares

SNLS can be used to estimate the nonlinear parameters corresponding to the flow separation states. SNLS is a subset of nonlinear least squares problems, characterized by the ability to separate the model into linear and nonlinear components, which reduces computational load compared to full nonlinear optimization [32]. This separation is possible due to the following structure:

$$\hat{\boldsymbol{Y}} = f_m(\boldsymbol{x}, \boldsymbol{c}, \boldsymbol{\theta}) = \boldsymbol{\Phi}(\boldsymbol{x}, \boldsymbol{\theta}) \cdot \boldsymbol{c} \tag{13}$$

Here, $\boldsymbol{c} \in \mathbb{R}^n$ is a set of linear parameters and $\boldsymbol{\theta} \in \mathbb{R}^k$ is a set of nonlinear parameters. Furthermore, $\boldsymbol{\Phi}$ is a regression matrix, which is a function of the aircraft state $\boldsymbol{x}$ and nonlinear parameters $\boldsymbol{\theta}$. The dependency on the aircraft state $\boldsymbol{x}$ will be dropped in further equations to be concise. Lastly, $\hat{\boldsymbol{Y}}$ are the estimated outputs of the model at each data point. As with any least squares problem, the cost function is the sum of the squared residuals:

$$\boldsymbol{L}(\boldsymbol{c},\boldsymbol{\theta}) = \|\boldsymbol{Y} - \boldsymbol{\Phi}(\boldsymbol{\theta}) \cdot \boldsymbol{c}\|^2 \tag{14}$$

Here, $\boldsymbol{Y}$ are the observed outputs at each data point. The structure allows for solving the linear parameters $\boldsymbol{c}$ as if it were an ordinary linear least squares problem. However, due to the dependency of $\boldsymbol{\Phi}$ on $\boldsymbol{\theta}$ the optimal estimate of $\boldsymbol{c}$ will also be dependent on $\boldsymbol{\theta}$. The least squares solution looks as follows:

$$\hat{\boldsymbol{c}}(\boldsymbol{\theta}) = \boldsymbol{\Phi}(\boldsymbol{\theta})^+ \cdot \boldsymbol{Y} \tag{15}$$

This optimal estimate can then be substituted in Eq. (14) which reduces the number of parameters to estimate from $n + k$ to k. Golub and Pereyra [31] proved that this reduction is valid and that when the reduced problem is solved for an optimal $\hat{\boldsymbol{\theta}}$ this also results in an optimal $\hat{\boldsymbol{c}}$, which minimizes the cost function globally. The reduced problem takes the following form:

$$\boldsymbol{L}(\boldsymbol{\theta}) = \|\boldsymbol{Y} - \boldsymbol{\Phi}(\boldsymbol{\theta}) \cdot \boldsymbol{\Phi}(\boldsymbol{\theta})^+ \cdot \boldsymbol{Y}\|^2 = \|\boldsymbol{P}^{\perp}_{\boldsymbol{\Phi}(\boldsymbol{\theta})} \cdot \boldsymbol{Y}\|^2 = \|\boldsymbol{r}(\boldsymbol{\theta})\|^2 \tag{16}$$

Here, $\boldsymbol{P}^{\perp}_{\boldsymbol{\Phi}(\boldsymbol{\theta})}$ signifies the projector onto the orthogonal complement of the column space of $\boldsymbol{\Phi}(\boldsymbol{\theta})$, defined as $\boldsymbol{I} - \boldsymbol{\Phi}(\boldsymbol{\theta})\boldsymbol{\Phi}(\boldsymbol{\theta})^+$. This effectively eliminates all contributions of the model proportional to the columns in $\boldsymbol{\Phi}(\boldsymbol{\theta})$, isolating the nonlinear contributions. Furthermore, $\boldsymbol{r}(\boldsymbol{\theta})$ is introduced as the residual vector, defined as $\boldsymbol{P}^{\perp}_{\boldsymbol{\Phi}(\boldsymbol{\theta})} \cdot \boldsymbol{Y}$.

The reduced problem can be solved with the nonlinear least squares tool in MATLAB[1]. This uses the trust-region-reflective method to find a minimum to the least squares problem. This method requires the formation of a Jacobian matrix, which provides the sensitivity of $\boldsymbol{r}(\boldsymbol{\theta})$ to the parameters $\boldsymbol{\theta}$. This is used to define the next step in the algorithm. The Jacobian of the residuals is defined in Eq. (17), where the dependency on $\boldsymbol{\theta}$ was dropped for convenience.

$$\mathbf{D}\boldsymbol{r} = -(\boldsymbol{P}^{\perp}_{\boldsymbol{\Phi}} \cdot \mathbf{D}\boldsymbol{\Phi}) \cdot \boldsymbol{\Phi}^+ \cdot \boldsymbol{Y} - (\boldsymbol{\Phi}^+)^\top \cdot (\boldsymbol{P}^{\perp}_{\boldsymbol{\Phi}} \cdot \mathbf{D}\boldsymbol{\Phi})^\top \cdot \boldsymbol{Y} \tag{17}$$

$\mathbf{D}$ defines the Fréchet derivative which is a generalization of derivatives in normed spaces [43]. This allows for the derivative of $\boldsymbol{\Phi}(\boldsymbol{\theta}) : \mathbb{R}^k \to \mathbb{R}^{(m \times n)}$ to be taken as $\mathbf{D}\boldsymbol{\Phi}(\boldsymbol{\theta}) : \mathbb{R}^k \to \mathbb{R}^{(m \times n \times k)}$ where $\mathbf{D}\boldsymbol{\Phi}(\boldsymbol{\theta})_{ijq} = \frac{\partial \Phi_{ij}(\boldsymbol{\theta})}{\partial \alpha_q}$. A novel expression for $\boldsymbol{D}\boldsymbol{r}$ equivalent to Eq. (17) that reduces memory storage is presented:

$$\mathbf{D}\boldsymbol{r} = -\mathbf{D}\boldsymbol{\Phi} \cdot \hat{\boldsymbol{c}} + \boldsymbol{\Phi} \cdot (\boldsymbol{\Phi}^+ \cdot (\mathbf{D}\boldsymbol{\Phi} \cdot \hat{\boldsymbol{c}})) - (\boldsymbol{\Phi}^+)^\top \cdot (\mathbf{D}\boldsymbol{\Phi})^\top \cdot \boldsymbol{r} \tag{18}$$

Proof. Equation (17) consists of two segments: $\boldsymbol{D}\boldsymbol{r} = -J_1 - J_2$. These segments can be refactored separately. Starting with J_1:

$$\begin{aligned}
J_1 &= (\boldsymbol{P}^{\perp}_{\boldsymbol{\Phi}} \cdot \mathbf{D}\boldsymbol{\Phi}) \cdot \boldsymbol{\Phi}^+ \cdot \boldsymbol{Y} \\
J_1 &= (\boldsymbol{P}^{\perp}_{\boldsymbol{\Phi}} \cdot \mathbf{D}\boldsymbol{\Phi}) \cdot \hat{\boldsymbol{c}} && (\hat{\boldsymbol{c}} = \boldsymbol{\Phi}^+ \cdot \boldsymbol{Y}) \\
J_1 &= ((\boldsymbol{I} - \boldsymbol{\Phi} \cdot \boldsymbol{\Phi}^+) \cdot \mathbf{D}\boldsymbol{\Phi}) \cdot \hat{\boldsymbol{c}} && (\boldsymbol{P}^{\perp}_{\boldsymbol{\Phi}} = \boldsymbol{I} - \boldsymbol{\Phi} \cdot \boldsymbol{\Phi}^+) \\
J_1 &= \mathbf{D}\boldsymbol{\Phi} \cdot \hat{\boldsymbol{c}} - \boldsymbol{\Phi} \cdot (\boldsymbol{\Phi}^+ \cdot (\mathbf{D}\boldsymbol{\Phi} \cdot \hat{\boldsymbol{c}})) && \text{(refactor)}
\end{aligned}$$

[1] https://nl.mathworks.com/help/optim/ug/lsqnonlin.html

Next, J_2 can be refactored:

$$
\begin{aligned}
J_2 &= (\boldsymbol{\Phi}^+)^\top \cdot (\boldsymbol{P}_{\boldsymbol{\Phi}}^\perp \cdot \mathbf{D}\boldsymbol{\Phi})^\top \cdot \boldsymbol{Y} \\
J_2 &= (\boldsymbol{Y}^\top \cdot \boldsymbol{P}_{\boldsymbol{\Phi}}^\perp \cdot \mathbf{D}\boldsymbol{\Phi} \cdot \boldsymbol{\Phi}^+)^\top && \text{(double transpose)} \\
J_2 &= (\boldsymbol{Y}^\top \cdot (I - \boldsymbol{\Phi} \cdot \boldsymbol{\Phi}^+) \cdot \mathbf{D}\boldsymbol{\Phi} \cdot \boldsymbol{\Phi}^+)^\top && (\boldsymbol{P}_{\boldsymbol{\Phi}}^\perp = I - \boldsymbol{\Phi} \cdot \boldsymbol{\Phi}^+) \\
J_2 &= ((\boldsymbol{Y}^\top - \boldsymbol{Y}^\top \cdot \boldsymbol{\Phi} \cdot \boldsymbol{\Phi}^+) \cdot \mathbf{D}\boldsymbol{\Phi} \cdot \boldsymbol{\Phi}^+)^\top && \text{(refactor)} \\
J_2 &= ((\boldsymbol{Y} - (\boldsymbol{\Phi} \cdot \boldsymbol{\Phi}^+)^\top \cdot \boldsymbol{Y})^\top \cdot \mathbf{D}\boldsymbol{\Phi} \cdot \boldsymbol{\Phi}^+)^\top && \text{(double transpose)} \\
J_2 &= ((\boldsymbol{Y} - \boldsymbol{\Phi} \cdot \boldsymbol{\Phi}^+ \cdot \boldsymbol{Y})^\top \cdot \mathbf{D}\boldsymbol{\Phi} \cdot \boldsymbol{\Phi}^+)^\top && ((\boldsymbol{\Phi} \cdot \boldsymbol{\Phi}^+)^\top = \boldsymbol{\Phi} \cdot \boldsymbol{\Phi}^+) \\
J_2 &= (\boldsymbol{r}^\top \cdot \mathbf{D}\boldsymbol{\Phi} \cdot \boldsymbol{\Phi}^+)^\top && (\boldsymbol{r} = \boldsymbol{Y} - \boldsymbol{\Phi} \cdot \boldsymbol{\Phi}^+ \cdot \boldsymbol{Y}) \\
J_2 &= (\boldsymbol{\Phi}^+)^\top \cdot (\mathbf{D}\boldsymbol{\Phi})^\top \cdot \boldsymbol{r} && \text{(refactor transpose)}
\end{aligned}
$$

Now by substituting J_1 and J_2:

$$
\begin{aligned}
\boldsymbol{D}\boldsymbol{r} &= -J_1 - J_2 \\
\boldsymbol{D}\boldsymbol{r} &= -\mathbf{D}\boldsymbol{\Phi} \cdot \hat{\boldsymbol{c}} + \boldsymbol{\Phi} \cdot (\boldsymbol{\Phi}^+ \cdot (\mathbf{D}\boldsymbol{\Phi} \cdot \hat{\boldsymbol{c}})) - (\boldsymbol{\Phi}^+)^\top \cdot (\mathbf{D}\boldsymbol{\Phi})^\top \cdot \boldsymbol{r}
\end{aligned}
$$

which proves that Eq. (18) is equivalent to Eq. (17).

□

Further inspiration is taken from Golub and Pereyra [31], and O'Leary and Rust [44], who suggest reducing the storage and computational constraints by bookkeeping the non-zero derivatives and skipping storing or calculating the zero derivatives.

The parameter variance can be determined to give a bound on the confidence one has in the estimated parameter values. Mahata and Söderström [45] present a method to estimate the parameter covariance matrix of the union of $\boldsymbol{c}$ and $\boldsymbol{\theta}$.

$$
Cov[\boldsymbol{\theta}, \boldsymbol{c}] = \left[\nabla f_m^\top \cdot \nabla f_m\right]^{-1} \left[\nabla f_m^\top \cdot \Lambda_m \cdot \nabla f_m\right] \left[\nabla f_m^\top \cdot \nabla f_m\right]^{-1} \tag{19}
$$

In Eq. (19), ∇f_m is the Jacobian matrix of f_m with respect to the parameters $\boldsymbol{\theta}$ and $\boldsymbol{c}$. Furthermore, Λ_m is a Toeplitz matrix built from the autocorrelation sequence $\{\lambda_t\}$ of the residuals r_t. Each diagonal D_i of Λ_m for $-m+1 \leq i \leq m-1$ is constant with value λ_i, where $D_i \neq D_0$ refers to the off-diagonals. The diagonal of the covariance matrix contains the parameter variances.

3.5 Linear Parameter Estimation

For the identification of aerodynamic coefficient models, linear parameter estimation is used. Linear parameter estimation deals with the identification of parameter values in equations that are linear in the parameters. Note that this does not require the regressors to be linear.

$$
\hat{\boldsymbol{Y}} = \boldsymbol{X}\boldsymbol{c} \tag{20}
$$

Equation (20) is the general form for this type of model, where $\boldsymbol{X}$ is the regression matrix and $\boldsymbol{c}$ is a vector containing the linear parameters. An estimate for the parameter values can be found using ordinary least squares.

$$
\hat{\boldsymbol{c}} = \boldsymbol{X}^+ \cdot \boldsymbol{Y} \tag{21}
$$

The covariance matrix is defined in Eq. (22) and comes from the system identification book by Klein and Morelli [46]. Here Λ_m has the same definition as in Section 3.4.

$$Cov[\boldsymbol{c}] = \left[\boldsymbol{X}^\top \cdot \boldsymbol{X}\right]^{-1} \left[\boldsymbol{X}^\top \cdot \Lambda_m \cdot \boldsymbol{X}\right] \left[\boldsymbol{X}^\top \cdot \boldsymbol{X}\right]^{-1} \tag{22}$$

3.6 Model Validation

As mentioned in Section 3.1, 20% of the flight data is reserved for validation. Two main statistics are calculated for the training and validation data sets to judge the performance of the models. First, the mean square error (MSE) is calculated. This value is calculated as follows:

$$MSE = \frac{\sum_{i=1}^{N}(y_i - \hat{y}_i)^2}{N} \tag{23}$$

Secondly, the coefficient of determination or R^2 value can be calculated. This value is an indication of the accuracy of the fit, where 1 indicates a perfect fit. Typically the value varies between 0 and 1, but it is possible to go below one when the measured signal has little variation. The value is calculated as follows:

$$R^2 = 1 - \frac{\sum_{i=1}^{N}(y_i - \hat{y}_i)^2}{\sum_{i=1}^{N}(y_i - \mu_y)^2} \tag{24}$$

4 Results

4.1 Evaluation of Separable Nonlinear Least Squares

To judge the effectiveness of SNLS, the model structure defined in Van Ingen et al. [30] is reidentified. In addition, the same data set and training-validation split are used, see Section 3.1 for details. Note that the cut-off frequencies are still different from the work of Van Ingen et al. [30]. Estimation of flow separation and lift coefficient parameters is performed using the SNLS method. The remaining coefficients are estimated using OLS.

The MSE values on the training and validation data are summarized in Table 7. The MSE values of the lift coefficient are reduced by 36% and 25% on the training and validation data respectively. This consistent reduction shows that the SNLS method finds better solutions within the same optimization problem. Moreover, the computation time is reduced from hours to seconds, which opens the door to more extensive iteration and analysis. All other MSE values of force and moment coefficients are reduced for the training data. However, this consistency is not found in the validation data. This indicates that the model structures might not be optimal, further exploration of different model structures is covered in Section 4.2.

4.2 Model Structure Selection

4.2.1 Flow Separation Model

As mentioned in Section 3.3, a second flow separation state is introduced to model the effects of the stall strips. For each flow separation state, the choice remains between a steady, a quasi-steady, and an unsteady flow separation model. In this section, an analysis is done to explore the different options. For this analysis, SNLS is performed on the lift coefficient. The presumed model incorporates a bias, two

Table 7 Comparison of mean square error values for the model defined by Van Ingen et al. [30] and unidentified using SNLS in this work.

	Training Data			Validation Data		
	Van Ingen	*This work*		*Van Ingen*	*This work*	
Model	**MSE**	**MSE**	**Difference** [%]	**MSE**	**MSE**	**Difference** [%]
C_L	2.74×10^{-3}	1.76×10^{-3}	−36	2.48×10^{-3}	1.86×10^{-3}	−25
C_D	1.33×10^{-4}	1.12×10^{-4}	−15	1.01×10^{-4}	1.00×10^{-4}	−1
C_X	1.65×10^{-4}	1.30×10^{-4}	−21	9.09×10^{-5}	9.28×10^{-5}	2
C_Z	2.70×10^{-3}	1.74×10^{-3}	−36	1.87×10^{-3}	1.87×10^{-3}	0
C_m	1.17×10^{-4}	1.08×10^{-4}	−8	1.25×10^{-4}	1.25×10^{-4}	0

Kirchhoff terms, a pitch rate term, and an elevator deflection term. The model looks as follows:

$$C_L = C_{L_0} + C_{L_{\alpha,ss}} \left(\frac{1 + \sqrt{X_{ss}}}{2} \right)^2 \alpha + C_{L_{\alpha,w}} \left(\frac{1 + \sqrt{X_w}}{2} \right)^2 \alpha + C_{L_{q^*}} \frac{q\bar{c}}{V} + C_{L_{\delta_e}} \delta_e \tag{25}$$

Here, X_{ss} is the flow separation state at the stall strip and X_w models the rest of the wing. For both X_{ss} and X_w the steady, quasi-steady and unsteady flow separation models are explored. This leads to nine potential model structures as seen in Table 8. The choice for lift model structure will be explained in Section 4.3.2.

Table 8 Mean square error fit of the lift model using different flow separation dynamics models for the stall strip and wing. The most accurate result is highlighted in green.

		Stall Strip X_{ss}		
		Steady	**Quasi-steady**	**Unsteady**
Wing X_w	**Steady**	3.73×10^{-3}	3.65×10^{-3}	3.55×10^{-3}
	Quasi-steady	3.73×10^{-3}	3.65×10^{-3}	3.56×10^{-3}
	Unsteady	3.70×10^{-3}	3.64×10^{-3}	3.69×10^{-3}

Examining the MSE values of the models in Table 8 reveals several key insights. First, the values are nearly identical when using either a steady or quasi-steady model for X_w. This is because the parameter $\tau_{2,w}$ approaches zero in the quasi-steady models, effectively reducing them to steady models. Furthermore, incorporating unsteady terms enhances the performance of the stall strip flow separation model, where the combination of two unsteady models is an exception. The exception is due to poor convergence, which may be caused by poor observability of the two τ_1 parameters. Consequently, an unsteady model is selected for X_{ss}, while a steady model is chosen for X_w. For the remainder of this paper, the unsteady model for X_{ss} and the steady model for X_w will be utilized as presented in Eqs. (26) and (27). The parameter estimation and associated statistics are presented in Section 4.3.1.

$$\tau_{1,ss} \frac{dX_{ss}}{dt} + X_{ss} = \frac{1}{2} - \frac{1}{2} \tanh \left(a_{1,ss} \left[\alpha - \tau_{2,ss} \dot{\alpha} - \alpha^*_{ss} \right] \right) \tag{26}$$

$$X_w = \frac{1}{2} - \frac{1}{2} \tanh \left(a_{1,w} \left[\alpha - \alpha^*_w \right] \right) \tag{27}$$

4.2.2 Lift Model

The lift model created by Van Ingen et al. [30], referred to as **Van Ingen CL**, serves as a baseline for comparison with the new model structures defined in this paper. As mentioned in Section 3.3.2, six lift coefficient models are proposed for comparison. **Model CL-I** and **Model CL-II** use one flow separation state, reconstructed using an unsteady flow separation model. **Model CL-III** through **Model CL-VI** use two flow separation states, where X_{ss} uses an unsteady flow separation model and X_w uses a flow steady separation model. The results of the parameter estimation can be summarized using the MSE on the training set. These results are presented in Table 9.

Table 9 Summary of the model exploration for the lift coefficient model. The underlying separation model types are defined as steady (S), quasi-steady (Q) or unsteady (U). Furthermore, the linear parameters are defined. Lastly, the MSE of the lift and normal force coefficient on the training data are also presented. The most accurate result is highlighted in green.

Model			MSE	
Name	**Separation Models (S/Q/U)**	**Linear Parameters**	C_L	C_Z
Van Ingen CL	U	$C_{L_0}, C_{L_\alpha}, C_{L_{\alpha^2}}$	5.2256×10^{-3}	5.0438×10^{-3}
Model CL-I	U	$C_{L_0}, C_{L_\alpha}, C_{L_{\alpha^2}}$	3.8823×10^{-3}	3.7420×10^{-3}
Model CL-II	U	C_{L_0}, C_{L_α}	3.9255×10^{-3}	3.7874×10^{-3}
Model CL-III	U | S	$C_{L_0}, C_{L_{\alpha,ss}}, C_{L_{\alpha,w}}$	3.7919×10^{-3}	3.6565×10^{-3}
Model CL-IV	U | S	$C_{L_0}, C_{L_{\alpha,ss}}, C_{L_{\alpha,w}}, C_{L_{q^*}}$	3.6244×10^{-3}	3.4975×10^{-3}
Model CL-V	U | S	$C_{L_0}, C_{L_{\alpha,ss}}, C_{L_{\alpha,w}}, C_{L_{\delta_e}}$	3.6448×10^{-3}	3.5150×10^{-3}
Model CL-VI	U | S	$C_{L_0}, C_{L_{\alpha,ss}}, C_{L_{\alpha,w}}, C_{L_{q^*}}, C_{L_{\delta_e}}$	3.5534×10^{-3}	3.4278×10^{-3}

As a first step, **Van Ingen CL** and **Model CL-I** are compared. This comparison is made to see the relative performance of the newly developed SNLS method compared to the old nonlinear parameter estimation method. The SNLS method shows a 25.7% reduction in training MSE. Next, **Model CL-II** shows the quadratic spline term is not of significant contribution compared to **Model CL-I** as removing it does not degrade model performance. Therefore, the spline term will be excluded from further analysis. Moving to the two flow separation states, **Model CL-III** shows a 3.4% reduction in training MSE compared to **Model CL-II**.

Another objective of the proposed model structures is the evaluation of pitch rate q and elevator deflection δ_e effects. This is done through model structures **Model CL-IV** through **Model CL-VI**, where **Model CL-IV** and **Model CL-V** evaluate the separate effects of the pitch rate and elevator deflection respectively, and **Model CL-VI** evaluates the combined effect. The results show that compared to **Model CL-III**, the pitch rate term reduces the training MSE by 4.4% and the elevator deflection term reduces the MSE by 3.9%. Combined the two terms reduce the MSE by 6.3%. The combination of SNLS, two flow separation states, and the inclusion of pitch rate and elevator deflection terms reduce the MSE with a total of 32%. The final model structure looks as follows:

$$C_L = C_{L_0} + C_{L_{\alpha,ss}} \left(\frac{1 + \sqrt{X_{ss}}}{2} \right)^2 \alpha + C_{L_{\alpha,w}} \left(\frac{1 + \sqrt{X_w}}{2} \right)^2 \alpha + C_{L_{q^*}} \frac{q\bar{c}}{V} + C_{L_{\delta_e}} \delta_e \tag{28}$$

4.2.3 Drag Model

A total of fourteen models have been tested for the drag model. This is done with five main objectives objectives defined in Section 3.3.3. The results of the comparisons are summarized in Table 10. Looking deeper into the results, interesting insights can be found. Starting with the direct comparison of the two

nonlinear parameter estimation methods. Using SNLS to estimate **Model CL-I** and then using OLS to estimate **Model CD-I** results in a 12.0% decrease in MSE for the drag coefficient. However, more importantly, the longitudinal force coefficient MSE is reduced by 54.7%. This larger improvement is due to the combined effects of the lift and drag coefficient model improvements.

Table 10 Summary of the model exploration for the drag coefficient model. The underlying lift coefficient model is referenced. Furthermore, the linear parameters are defined. Lastly, the MSE of the lift and normal force coefficient on the training data are also presented. The most accurate result is highlighted in green.

Model			MSE	
Name	**Lift Model**	**Linear Parameters**	C_D	C_X
Van Ingen CD	**Van Ingen CL**	$C_{D_0}, C_{D_\alpha}, C_{D_{\delta_e}}, C_{D_{C_T}}, C_{D_X}$	2.3514×10^{-4}	4.1277×10^{-4}
Model CD-I	**Model CL-I**	$C_{D_0}, C_{D_\alpha}, C_{D_{\delta_e}}, C_{D_{C_T}}, C_{D_X}$	2.1027×10^{-4}	1.9151×10^{-4}
Model CD-II	**Model CL-VI**	$C_{D_0}, C_{D_\alpha}, C_{D_{\delta_e}}, C_{D_{C_T}}, C_{D_{X,ss}}, C_{D_{X,w}}$	1.7545×10^{-4}	1.2495×10^{-4}
Model CD-III	**Model CL-VI**	$C_{D_0}, C_{D_{C_T}}, C_{D_{q^*}}, C_{D_{\delta_e}}, C_{D_{X,ss}}, C_{D_{X,w}}$	1.7890×10^{-4}	1.2814×10^{-4}
Model CD-IV	**Model CL-VI**	$C_{D_0}, C_{D_{C_T}}, C_{D_{q^*}}, C_{D_{\delta_e}}, C_{D_{X,ss}}, C_{D_{X,w}}, C_{D_\alpha}$	1.7225×10^{-4}	1.2372×10^{-4}
Model CD-V	**Model CL-VI**	$C_{D_0}, C_{D_{C_T}}, C_{D_{q^*}}, C_{D_{\delta_e}}, C_{D_{X,ss}}, C_{D_{X,w}}, C_{D_{\alpha^2}}$	1.6585×10^{-4}	1.1980×10^{-4}
Model CD-VI	**Model CL-VI**	$C_{D_0}, C_{D_{C_T}}, C_{D_{q^*}}, C_{D_{\delta_e}}, C_{D_{X,ss}}, C_{D_{X,w}}, C_{D_\alpha}, C_{D_{\alpha^2}}$	1.6162×10^{-4}	1.1749×10^{-4}
Model CD-VII	**Model CL-VI**	$C_{D_0}, C_{D_{C_T}}, C_{D_{q^*}}, C_{D_{\delta_e}}, C_{D_{X,ss}}, C_{D_{X,w}}, C_{D_{C_L}}$	1.7186×10^{-4}	1.2327×10^{-4}
Model CD-VIII	**Model CL-VI**	$C_{D_0}, C_{D_{C_T}}, C_{D_{q^*}}, C_{D_{\delta_e}}, C_{D_{X,ss}}, C_{D_{X,w}}, C_{D_{C_L^2}}$	1.6683×10^{-4}	1.1981×10^{-4}
Model CD-IX	**Model CL-VI**	$C_{D_0}, C_{D_{C_T}}, C_{D_{q^*}}, C_{D_{\delta_e}}, C_{D_{X,ss}}, C_{D_{X,w}}, C_{D_{C_L}}, C_{D_{C_L^2}}$	1.6077×10^{-4}	1.1572×10^{-4}
Model CD-X	**Model CL-VI**	$C_{D_0}, C_{D_{C_T}}, C_{D_{q^*}}, C_{D_{\delta_e}}, C_{D_{C_L}}$	4.7955×10^{-4}	4.0464×10^{-4}
Model CD-XI	**Model CL-VI**	$C_{D_0}, C_{D_{C_T}}, C_{D_{q^*}}, C_{D_{\delta_e}}, C_{D_{C_L^2}}$	4.5693×10^{-4}	3.8668×10^{-4}
Model CD-XII	**Model CL-VI**	$C_{D_0}, C_{D_{C_T}}, C_{D_{q^*}}, C_{D_{\delta_e}}, C_{D_{C_L}}, C_{D_{C_L^2}}$	4.0461×10^{-4}	3.4206×10^{-4}
Model CD-XIII	**Model CL-VI**	$C_{D_0}, C_{D_{C_T}}, C_{D_{q^*}}, C_{D_{\delta_e}}, C_{D_{K_D,ss}}, C_{D_{K_D,w}}$	2.6119×10^{-4}	2.0720×10^{-4}
Model CD-XIV	**Model CL-VI**	$C_{D_0}, C_{D_{C_T}}, C_{D_{q^*}}, C_{D_{\delta_e}}, C_{D_{X,ss}}, C_{D_{X,w}}, C_{D_{K_D,ss}}, C_{D_{K_D,w}}$	1.7722×10^{-4}	1.2555×10^{-4}

Moving on to objective number two, the addition of a second flow separation state. Compared to **Model CD-I**, **Model CD-II** further decreases the drag coefficient MSE by 15.6%. This in combination with the improved lift model **Model CL-VI** causes a 34.0% reduction of the longitudinal force coefficient MSE.

The next goal is to review the contribution of the angle of attack as a direct regressor in the model. Before analyzing this, a baseline is set with **Model CD-III**. Then, **Model CD-IV** and **Model CD-V** are

estimated to see the improvements of including α and α^2, respectively. Furthermore, **Model CD-VI** shows the effect of including both. It is seen that α^2 has a more significant effect than α, but the best effect is seen when combining the terms. **Model CD-VI** makes a 9.7% reduction in drag coefficient MSE and 8.5% reduction in longitudinal force coefficient MSE, all compared to baseline **Model CD-III**.

A very similar analysis is done for the dependency of drag on lift. **Model CD-III** is used as a baseline. A first observation can be made by looking at **Model CD-X** through **Model CD-XII**. Due to their poor performance, these models are discarded. Looking at **Model CD-VII** through **Model CD-IX** the inclusion of only C_L, only C_L^2, and both are tested. The term C_L^2 outperforms C_L and including both works best. Furthermore, they show that the addition of $(1 - X_{ss})$ and $(1 - X_w)$ have significant impact. **Model CD-IX** reduces the drag coefficient MSE by 10.3% and longitudinal force coefficient by 10.0%, compared to **Model CD-III**. It can thus be said that the lift coefficient addition performs better than the angle of attack addition.

Lastly, the effect of the Kirchhoff flow term is tested and compared to **Model CD-III**. The results again show that the inclusion of $(1 - X_{ss})$ and $(1 - X_w)$ is necessary. The best performing version, **Model CD-XIV**, shows a 1.1% reduction in drag coefficient MSE and 2.1% reduction in longitudinal force coefficient MSE. This term performs worse than previous terms and is hence discarded.

From the previous analysis, **Model CD-IX** is selected for further refinement. Firstly, the pitch rate term is removed as its t-test null hypothesis was accepted. Looking further, the correlations between $C_{D_{C_L}}$ and $C_{D_{C_L^2}}$ as well as $C_{D_{C_L}}$ and C_{D_0} are between 0.8 and 0.9. Considering the small difference in performance between **Model CD-IX** and **Model CD-VIII**, the $C_{D_{C_L}}$ term is removed. This leads to the following model:

$$C_D = C_{D_0} + C_{D_{C_T}} C_T + C_{D_{\delta_e}} \delta_e + C_{D_{C_L^2}} C_L^2 + C_{D_{X,ss}} (1 - X_{ss}) + C_{D_{X,w}} (1 - X_w) \tag{29}$$

4.2.4 Pitch Moment Model

As mentioned in Section 3.3.4, 59 new model structures are selected to be evaluated for the pitch moment model. Due to their large quantity, individual mentions are omitted. However, global observations are discussed, and a comprehensive overview of all model fitting results is provided in Table 20 in Appendix B. The first objective was to estimate **Model Cm-I**, building on the results of **Model CL-I**. It decreases the MSE on the pitch moment coefficient by 2.3%.

Moving on to the models proposed by Leishman and Beddoes [35], and Singh and Jategaonkar [16]. First, it is observed that the inclusion of K_2^m does not provide significant improvements. Although marginal improvements are found, it is chosen to neglect these terms because of their diminishing returns and risk of overfitting. Furthermore, the inclusion of K_0 must be paired with K_1 or $(1 - X)$ to provide good results.

The model term proposed by Goman and Khrabrov [34], and Singh and Jategaonkar [16], shows poor performance individually. Paired with K_0 and $(1 - X)$ it provides a decent improvement. However, there is no clear physical underlying meaning for this. To improve the interpretability of the results, this term is omitted. Lastly, the inclusion of $X\delta_e$ to model a reduction in the elevator effectiveness at high angles of attack shows consistent improvements in the model. For this reason, it is chosen to keep it in the model.

Based on the previous sections, **Model Cm-XXXIII** is chosen. This model includes K_0 and K_1 as well as $X\delta_e$. Although the addition of $(1 - X)$ could improve the model slightly, it is excluded to limit the complexity of the model. **Model Cm-XXXIII** serves as a start for refinement. As a first observation, the correlation between $C_{m_{\delta_e}}$ and $C_{m_{X_w \delta_e}}$ is found to be above 0.9. Therefore, it is decided to remove the latter. This does not have significant repercussions in terms of model performance. This results in the

following model:

$$C_m = C_{m_0} + C_{m_{C_T}} C_T + C_{m_{q^*}} \frac{q\bar{c}}{V} + C_{m_{\delta_e}} \delta_e + C_{m_{c.g.}} \frac{x_{c.g.}}{\bar{c}} C_L \\ + C_{m_{K_0}} C_L + C_{m_{K_{1,ss}}} (1 - X_{ss}) C_L + C_{m_{K_{1,w}}} (1 - X_w) C_L + C_{m_{X_{ss}\delta_e}} X_{ss} \delta_e \tag{30}$$

Finally, by grouping the terms relating to C_L, a model for the distance between the center of gravity and the center of pressure can be obtained, this is referred to as $l_{c.p.}$. Furthermore, terms relating to the elevator deflection δ_e can be grouped to create a model of the effectivity of the elevator $C^*_{m_{\delta_e}}$. This results in the following model:

$$C_m = C_{m_0} + C_{m_{C_T}} C_T + C_{m_{q^*}} \frac{q\bar{c}}{V} - l_{c.p.} C_L + C^*_{m_{\delta_e}} \delta_e \tag{31}$$

$$l_{c.p.} = \frac{x_{c.p.} - x_{c.g.}}{\bar{c}} = -C_{m_{K_0}} - C_{m_{K_{1,ss}}} (1 - X_{ss}) - C_{m_{K_{1,w}}} (1 - X_w) - C_{m_{c.g.}} \frac{x_{c.g}}{\bar{c}} \tag{32}$$

$$C^*_{m_{\delta_e}} = C_{m_{\delta_e}} + C_{m_{X_{ss}\delta_e}} X_{ss} \tag{33}$$

4.3 Stall Model

The final model structure, as derived from the analyses described in Section 4.2, can be obtained as:

$$C_L = C_{L_0} + C_{L_{\alpha,ss}} \left(\frac{1 + \sqrt{X_{ss}}}{2} \right)^2 \alpha + C_{L_{\alpha,w}} \left(\frac{1 + \sqrt{X_w}}{2} \right)^2 \alpha + C_{L_{q^*}} \frac{q\bar{c}}{V} + C_{L_{\delta_e}} \delta_e \tag{34}$$

$$C_D = C_{D_0} + C_{D_{C_T}} C_T + C_{D_{\delta_e}} \delta_e + C_{D_{C_L^2}} C_L^2 + C_{D_{X,ss}} (1 - X_{ss}) + C_{D_{X,w}} (1 - X_w) \tag{35}$$

$$C_m = C_{m_0} + C_{m_{C_T}} C_T + C_{m_{q^*}} \frac{q\bar{c}}{V} - l_{c.p.} C_L + C^*_{m_{\delta_e}} \delta_e \tag{36}$$

The models for the aerodynamic force and moment coefficients are supplemented with a model for the position of the center of pressure and control effectiveness of the elevator:

$$l_{c.p.} = -C_{m_{K_0}} - C_{m_{K_{1,ss}}} (1 - X_{ss}) - C_{m_{K_{1,w}}} (1 - X_w) - C_{m_{c.g.}} \frac{x_{c.g}}{\bar{c}} \tag{37}$$

$$C^*_{m_{\delta_e}} = C_{m_{\delta_e}} + C_{m_{X_{ss}\delta_e}} X_{ss} \tag{38}$$

Lastly, the stall is modeled using two flow separation states. One state will model the effect of stall strips installed on the wing, and another will model the rest of the wing. The governing equations are obtained as:

$$\tau_{1,ss} \frac{dX_{ss}}{dt} + X_{ss} = \frac{1}{2} - \frac{1}{2} \tanh \left(a_{1,ss} \left[\alpha - \tau_{2,ss} \dot{\alpha} - \alpha^*_{ss} \right] \right) \tag{39}$$

$$X_w = \frac{1}{2} - \frac{1}{2} \tanh \left(a_{1,w} \left[\alpha - \alpha^*_w \right] \right) \tag{40}$$

4.3.1 Flow Separation Models

Using the SNLS method, the models for the lift coefficient and flow separation states defined in Eqs. (34), (39) and (40) can be estimated simultaneously. The results of this system identification task can be found in Tables 11 and 12. The results in Table 11 show an acceptable parameter standard deviation. It also shows that all null hypotheses for the t-test are rejected. Furthermore, all parameter

correlations in Table 12 are below 0.9. The correlation between $\tau_{1,ss}$ and $\tau_{2,ss}$ is very low, indicating that the new flight maneuvers mentioned in Section 3.1 are effective. The highest correlation is found for C_{L_0} and $C_{L_{\alpha,ss}}$. This correlation was already highlighted by Van Ingen et al. [30] and is likely caused by parts of the data having insufficient variation in the angle of attack. However, removing either term significantly reduces the accuracy of the model, thus both are retained.

Table 11 Parameter estimates and statistics for the final lift coefficient model. For the t-test $\circ$ indicates that the null hypothesis is accepted and $*$ that the null hypothesis is rejected.

		Results		t-test	
Parameter	**Unit**	$\hat{\theta}$	σ_θ	p	h
$\tau_{1,ss}$	s	**0.4191**	0.0722	0.0000	*
$\tau_{2,ss}$	s	**0.3391**	0.0346	0.0000	*
$a_{1,ss}$	-	**70.2846**	11.2205	0.0000	*
α^*_{ss}	rad	**0.1956**	0.0017	0.0000	*
$a_{1,w}$	-	**13.9276**	1.4462	0.0000	*
α^*_w	rad	**0.3267**	0.0056	0.0000	*
C_{L_0}	-	**0.2318**	0.0116	0.0000	*
$C_{L_{K_{\alpha,ss}}}$	-	**1.3851**	0.1061	0.0000	*
$C_{L_{K_{\alpha,w}}}$	-	**2.5961**	0.0536	0.0000	*
$C_{L_{q^*}}$	-	**8.0747**	1.3881	0.0000	*
$C_{L_{\delta_e}}$	-	**−0.3403**	0.0681	0.0000	*

Table 12 Parameter correlation matrix for the final lift coefficient model. High correlations are highlighted red.

	$\tau_{1,ss}$	$\tau_{2,ss}$	$a_{1,ss}$	α^*_{ss}	$a_{1,w}$	α^*_w	C_{L_0}	$C_{L_{K_{\alpha,ss}}}$	$C_{L_{K_{\alpha,w}}}$	$C_{L_{q^*}}$	$C_{L_{\delta_e}}$
$\tau_{1,ss}$	1.00	0.06	0.21	0.10	0.15	0.03	0.16	-0.35	0.33	0.06	-0.08
$\tau_{2,ss}$	0.06	1.00	-0.07	-0.35	0.09	0.36	0.09	-0.27	0.40	0.51	0.16
$a_{1,ss}$	0.21	-0.07	1.00	0.36	-0.08	0.03	0.07	0.04	-0.07	0.05	0.13
α^*_{ss}	0.10	-0.35	0.36	1.00	-0.04	0.04	0.17	-0.10	-0.26	-0.03	-0.21
$a_{1,w}$	0.15	0.09	-0.08	-0.04	1.00	0.30	0.00	-0.05	0.14	0.29	0.10
α^*_w	0.03	0.36	0.03	0.04	0.30	1.00	0.07	-0.16	0.28	0.46	0.21
C_{L_0}	0.16	0.09	0.07	0.17	0.00	0.07	1.00	-0.87	-0.27	0.58	-0.12
$C_{L_{K_{\alpha,ss}}}$	-0.35	-0.27	0.04	-0.10	-0.05	-0.16	-0.87	1.00	-0.11	-0.61	0.23
$C_{L_{K_{\alpha,w}}}$	0.33	0.40	-0.07	-0.26	0.14	0.28	-0.27	-0.11	1.00	0.25	0.49
$C_{L_{q^*}}$	0.06	0.51	0.05	-0.03	0.29	0.46	0.58	-0.61	0.25	1.00	0.30
$C_{L_{\delta_e}}$	-0.08	0.16	0.13	-0.21	0.10	0.21	-0.12	0.23	0.49	0.30	1.00

Looking at the static flow separation parameters of the stall strip and wing, a few observations can be made. Starting with the stall strip angle of attack α^*_{ss}. This is found to be at 11.2° and is in line with the start of buffet vibrations. Furthermore, the abruptness of the stall modeled by $a_{1,ss}$ is high. This corresponds well with the behavior of a stall strip, which causes flow separation at the leading edge. A high abruptness is seen here as a crude method for modeling a leading-edge stall. Moving on to $a_{1,w}$, a much more subtle stall is estimated for the rest of the wing. This is in line with the expected trailing-edge stall. Furthermore, α^*_w is estimated to be 18.7°. This corresponds well with the wind tunnel results for NACA23012, which indicated that the stall angle of attack must be between 15° and 20°.

Using the four static flow separation parameters discussed before, the static flow separation curves can be plotted. These are presented in the left plots of Fig. 6. Three main stages in the flow separation

behavior can be defined: no flow separation, stall strip flow separation, and full flow separation. No flow separation is the expected stage during normal flight, this is defined in Fig. 6 as stage 1. As can be seen in the top right plot, the flow separation line is located at the trailing edge of the wing. Moving on to stage 2, stall strip separation, corresponds to the middle right plot. It can be seen that the green flow separation line has moved to the leading edge which means full flow separation at the stall strips. Lastly, stage 3 refers to full flow separation and is shown in the bottom right plot. At this stage, the rest of the wing follows the stall strips and the flow separates.

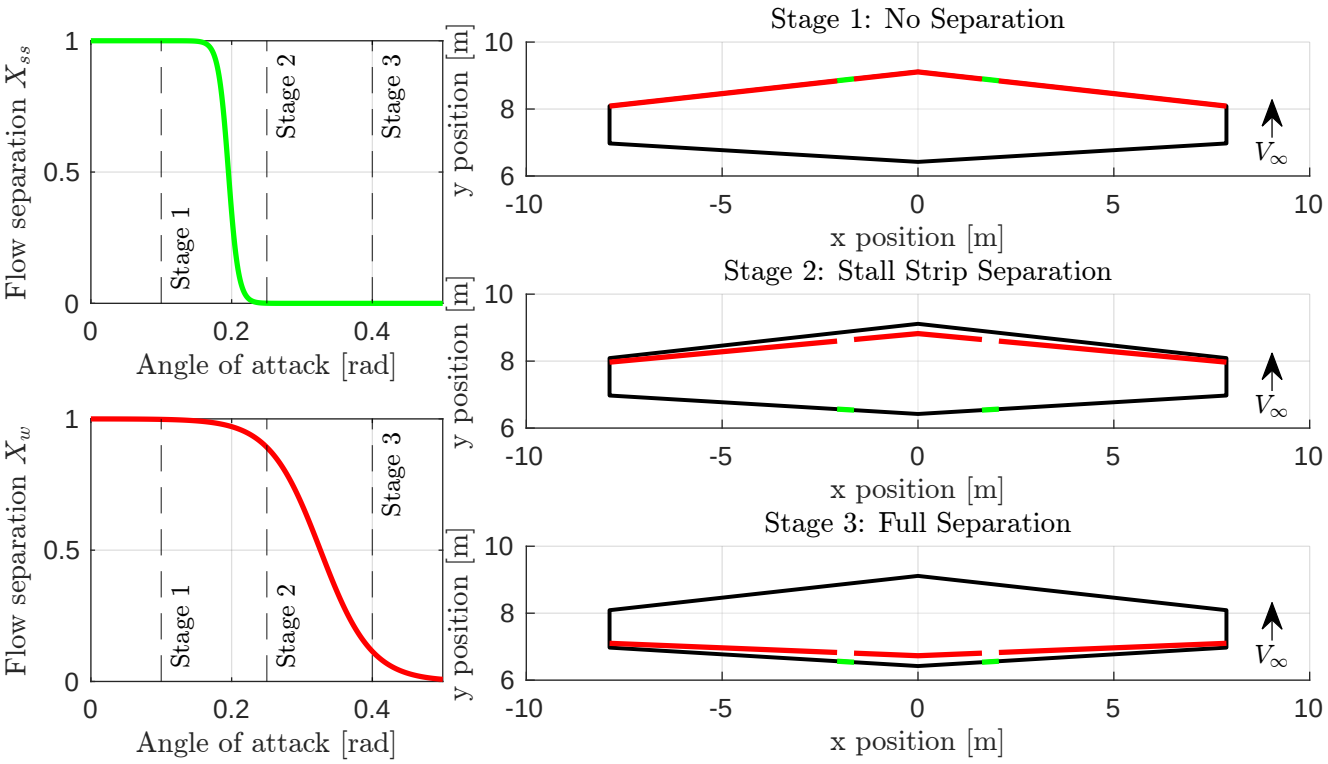

Fig. 6 Visualization of the stages of flow separation on the wing. Flow separation state of the stall strip in the top left plot. Flow separation state of the rest of the wing in the bottom left plot. The three right plots show the three stages of flow separation on a top view of the wing and reference the vertical lines in the left plots.

The unsteady flow separation parameters of the stall strip were determined at $\tau_{1,ss}$=0.4191 s and $\tau_{2,ss}$=0.3391 s. Using the average airspeed of the training set V=87 m/s and chord length, the non-dimensional time constants can be determined. These are $\tau^*_{1,ss}$=18.14 and $\tau^*_{2,ss}$=14.67. The value for $\tau_{1,ss}$ corresponds well with literature. However, $\tau_{2,ss}$ is observed to be relatively high [15].

4.3.2 Lift Model

The lift coefficient model parameters have been identified with SNLS in Section 4.3.1. A review of the parameter values in Table 11 is performed here. The zero angle of attack lift coefficient C_{L_0} is estimated at 0.2318. It is expected for this value to be above zero due to an angle of incidence of the wing and a camber in the airfoil profile. The lift curve slope in the linear part of the angle of attack range is 3.98 and found by combining $C_{L_{\alpha,ss}}$ and $C_{L_{\alpha,w}}$. The response of the lift to a pitch, captured by $C_{L_{q^*}}$, is positive, as expected. Lastly, the response of the lift to an elevator deflection is estimated to be negative. The low lift curve slope and negative response of lift to elevator deflection could be explained by a high correlation between the angle of attack and elevator deflection, which is estimated at -0.8 for the training set.

Using C_{L_0}, $C_{L_{\alpha,ss}}$, $C_{L_{\alpha,w}}$ and the steady flow separation parameters, the static lift curve can be constructed. Figure 7 shows the measured values as data points and the static lift curves of Van Ingen

[23] and this work. It can be seen that the measured values show significant spread, which can be attributed to neglected elevator deflection effects through $C_{L_{\delta_e}}$ and unsteady effects modeled by $\tau_{1,ss}$, $\tau_{2,ss}$ and $C_{L_{q^*}}$. Beyond that, it can be seen that both models are in the middle of the measurements in the low angle of attack regions. However, the previous model starts to diverge at high angles of attack due to the quadratic spline term in the work of Van Ingen [23]. This divergence already starts around 0.3 radians. On the other hand, the old model closer approximates the data at low angles of attack.

4.3.3 Drag Model

For the refined C_D model defined in Eq. (35), referred to as **Model CD-IXr**, the results of the parameter estimation are presented in Tables 13 and 14. It can be seen in Table 13 that all t-test null hypotheses are rejected, indicating that each parameter is significantly different from zero. Furthermore, it can be seen in Table 14 that all correlations are below 0.8.

Looking at the values of the coefficients, C_{D_0} is estimated at 0.0165, indicating there is some drag, even when all other contributions are zero. The coefficient $C_{D_{C_T}}$, which represents the derivative of drag with respect to the thrust coefficient, is estimated at 0.3917, which corresponds well with previous results found by Van Ingen et al. [30]. The coefficient for the elevator deflection $C_{D_{\delta_e}}$ is found to be negative. This is likely because the deflection is on average negative, which makes the contribution of the elevator to the drag positive. As expected, the lift causes added lift-induced drag, thus the coefficient $C_{D_{C_L^2}}$ is positive. The coefficients $C_{D_{X_{ss}}}$ and $C_{D_{X_w}}$ indicate that as the flow separates a further increase in drag is observed.

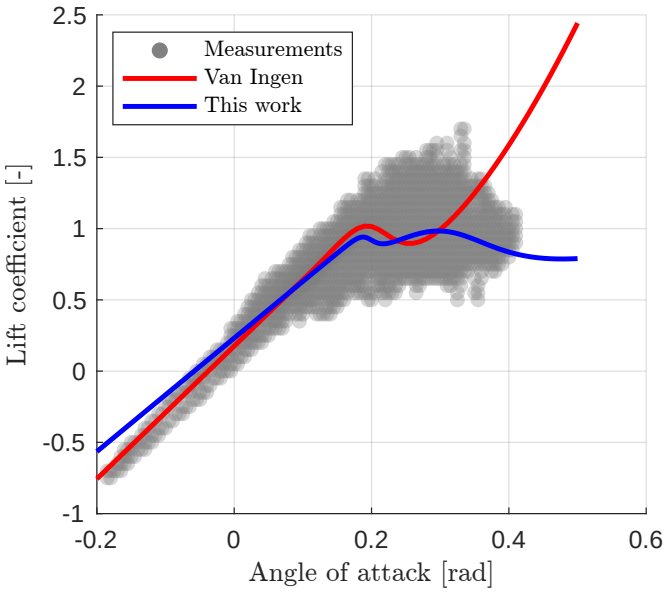

Fig. 7 Static lift curve for Van Ingen CL and Model CL-VI plotted over the measured lift coefficient values

Table 13 Estimated coefficients for the Drag coefficient model. For the t-test $\circ$ indicates that the null hypothesis is accepted and $*$ that the null hypothesis is rejected.

		Results		t-test	
Parameter	**Unit**	$\hat{\theta}$	$\sigma_{\hat{\theta}}$	p	h
C_{D_0}	-	**0.0165**	0.0020	0.0000	*
$C_{D_{C_T}}$	-	**0.3917**	0.0135	0.0000	*
$C_{D_{\delta_e}}$	-	**−0.1894**	0.0131	0.0000	*
$C_{D_{C_L^2}}$	-	**0.0258**	0.0035	0.0000	*
$C_{D_{X_{ss}}}$	-	**0.0555**	0.0017	0.0000	*
$C_{D_{X_w}}$	-	**0.2062**	0.0064	0.0000	*

Using the estimated model, the static drag polar may be constructed. The static drag polar is presented in Fig. 8. The polar is complemented by the measurements corrected for the effects of the thrust coefficient and elevator deflection. Furthermore, the model **Van Ingen CD** from Van Ingen et al. [30] is added for comparison. It can be seen that the new model better matches the high and low angle of attack regions. Furthermore, the C_L^2 term ensures that drag remains positive for negative angles of attack.

Table 14 Parameter correlation matrix for the Drag coefficient model.

	C_{D_0}	$C_{D_{C_T}}$	$C_{D_{\delta e}}$	$C_{D_{C_L^2}}$	$C_{D_{X_{ss}}}$	$C_{D_{X_w}}$
C_{D_0}	1.00	-0.74	-0.23	-0.76	0.20	0.40
$C_{D_{C_T}}$	-0.74	1.00	-0.05	0.23	0.14	-0.38
$C_{D_{\delta e}}$	-0.23	-0.05	1.00	0.73	-0.25	-0.04
$C_{D_{C_L^2}}$	-0.76	0.23	0.73	1.00	-0.40	-0.25
$C_{D_{X_{ss}}}$	0.20	0.14	-0.25	-0.40	1.00	-0.52
$C_{D_{X_w}}$	0.40	-0.38	-0.04	-0.25	-0.52	1.00

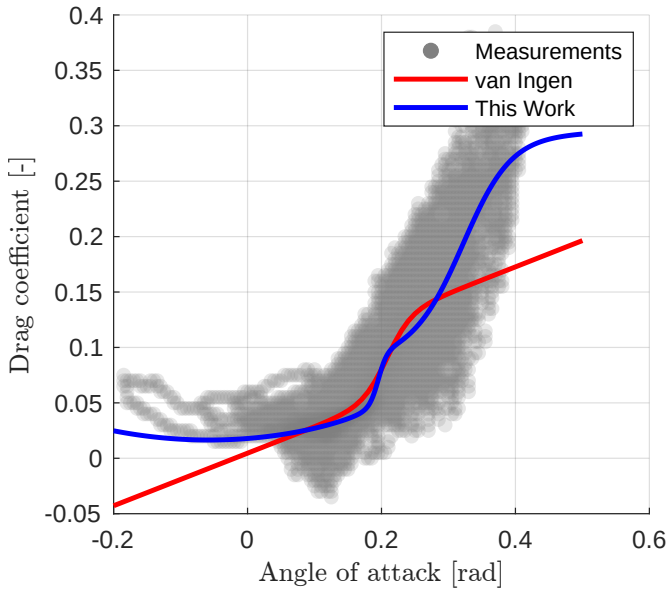

Fig. 8 Static drag polar for Van Ingen CL and Model CD-IXr plotted over the adjusted drag coefficient measurements

4.3.4 Pitch Moment Model

The results of the model identification for the pitch moment model in Eq. (36), referred to as **Model Cm-XXXIIIr**, are presented in Tables 15 and 16. Immediately, the high correlation between $C_{m_{cg}}$ and $C_{m_{K_0}}$ in Table 16 stands out. This makes sense as the center of gravity is relatively constant. However, due to the difference it makes for the accuracy of the model the term is retained. Beyond that, all terms were found to be significant by the t-test, and parameter correlations are below 0.8.

The model for the center of pressure is presented in Fig. 9. The center of pressure is measured from a datum defined 15 inches in front of the aircraft [33]. It can be seen that for low angles of attack, the center of pressure is constant and it shifts backward as the aircraft stalls. The stall angles of attack for the stall strip and the rest of the wing are highlighted in the figure. The shift back is expected and relates to the relative contribution of the horizontal tail becoming larger. The center of gravity envelope lies between 276 and 286 inches[2], which is ahead of the center of pressure at all times. This means that the configuration is stable; that this comes back from the identification results is an important marker for the reliability of the results.

Moving to the effective elevator control effectiveness $C^*_{m_{\delta_e}}$. It has long been known that the stall would adversely affect this [30]. The results in this work, as seen in Fig. 10, show the same. The initial control effectiveness is close to that estimated by Van Ingen et al. [30], however, the degradation is less.

[2]Information received from the TU Delft's research aircraft technicians

Table 15 Estimated coefficients for the Pitch moment coefficient model. For the t-test $\circ$ indicates that the null hypothesis is accepted and $*$ that the null hypothesis is rejected.

		Results		t-test	
Parameter	**Unit**	$\hat{\theta}$	$\sigma_{\hat{\theta}}$	p	h
C_{m_0}	-	0.0659	0.0026	0.0000	*
$C_{m_{C_T}}$	-	0.0794	0.0089	0.0000	*
$C_{m_{q^*}}$	-	−1.7502	0.2675	0.0000	*
$C_{m_{\delta_e}}$	-	−0.7431	0.0134	0.0000	*
$C_{m_{c.g.}}$	-	−0.9616	0.1305	0.0000	*
$C_{m_{K_0}}$	-	3.2316	0.4594	0.0000	*
$C_{m_{K_{1,ss}}}$	-	−0.0517	0.0033	0.0000	*
$C_{m_{K_{1,w}}}$	-	−0.0681	0.0053	0.0000	*
$C_{m_{X_1\delta_e}}$	-	−0.2576	0.0224	0.0000	*

Table 16 Parameter correlation matrix for the Pitch moment coefficient model. High correlations are highlighted red.

	C_{m_0}	$C_{m_{C_T}}$	$C_{m_{q^*}}$	$C_{m_{\delta_e}}$	$C_{m_{c.g.}}$	$C_{m_{K_0}}$	$C_{m_{K_{1,ss}}}$	$C_{m_{K_{1,w}}}$	$C_{m_{X_1\delta_e}}$
C_{m_0}	1.00	-0.41	0.54	0.07	-0.07	0.06	0.51	0.20	-0.38
$C_{m_{C_T}}$	-0.41	1.00	0.08	-0.07	-0.45	0.45	0.03	-0.30	0.08
$C_{m_{q^*}}$	0.54	0.08	1.00	0.28	-0.40	0.39	0.57	-0.23	-0.21
$C_{m_{\delta_e}}$	0.07	-0.07	0.28	1.00	-0.08	0.08	0.67	0.04	-0.68
$C_{m_{c.g.}}$	-0.07	-0.45	-0.40	-0.08	1.00	-1.00	-0.27	0.13	0.11
$C_{m_{K_0}}$	0.06	0.45	0.39	0.08	-1.00	1.00	0.26	-0.13	-0.11
$C_{m_{K_{1,ss}}}$	0.51	0.03	0.57	0.67	-0.27	0.26	1.00	-0.15	-0.78
$C_{m_{K_{1,w}}}$	0.20	-0.30	-0.23	0.04	0.13	-0.13	-0.15	1.00	-0.27
$C_{m_{X_1\delta_e}}$	-0.38	0.08	-0.21	-0.68	0.11	-0.11	-0.78	-0.27	1.00

In previous work, the degradation was forced to be 50%, due to the model structure. In this work, the identification has more freedom and therefore is seen as a more reliable estimate.

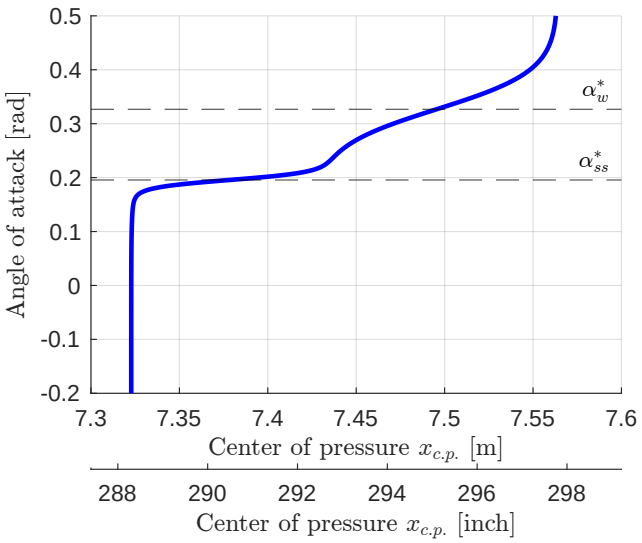

Fig. 9 Variation of the center of pressure $x_{c.p}$ with respect to a datum in front of the aircraft for increasing angle of attack.

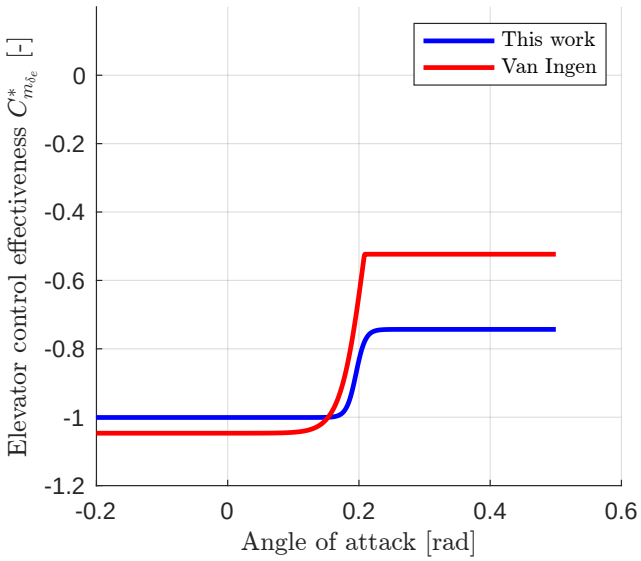

Fig. 10 Variation of the elevator control effectiveness for increasing angle of attack. Compared against Van Ingen et al. [30]

Lastly, the static pitch moment behavior can be plotted in Fig. 11. To do this, unsteady effects from the flow separation states are neglected. Furthermore, the measurements are corrected for elevator and thrust coefficient effects. The static pitch moment is compared to that obtained by Van Ingen et al. [30]. Interestingly, the two models behave very similarly in the low angle of attack region. However, for high angles of attack the new model levels off, as opposed to the previous model. This is expected as the lift, causing the moment, levels off as well. At first, this is offset by the shift of the center of pressure, but as that stabilizes the pitch moment settles too.

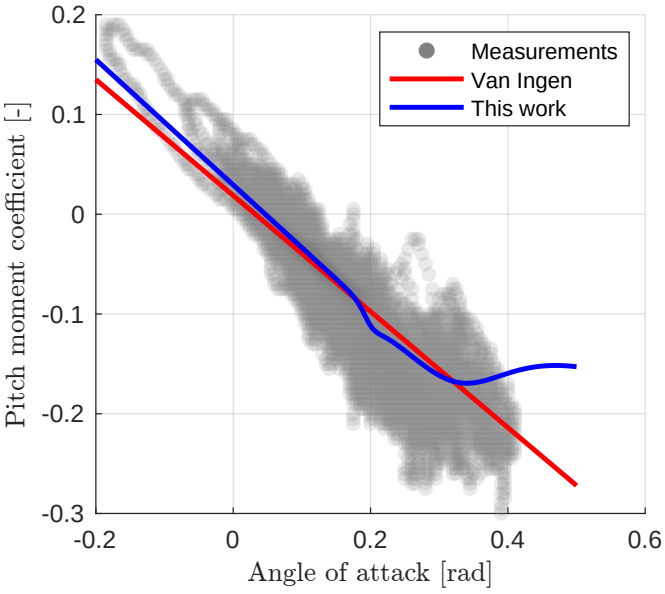

Fig. 11 Static pitch moment for Van Ingen Cm and Model Cm-XXXIIIr plotted over the adjusted pitch moment measurements.

4.4 Model Validation

As mentioned in Section 3.1, 20% of the data is saved to be used for validation. This data is used to show that the identified model can generalize. A comparison of the MSE values on the training and validation data sets is summarized in Table 17. This table recaps the reductions mentioned in previous sections. Furthermore, the reductions for the validation set are presented. Improvements for the validation set are smaller, but significant nonetheless. The consistency of the improvements builds confidence in the validity of the model.

The R^2 value can be calculated for each maneuver in the training and validation data sets. Moreover, the R^2 values can be obtained for all models. The resulting values are summarized in Fig. 12, where Fig. 12a shows the training data and Fig. 12b shows the validation data. The plots show an improvement in the consistency of the model obtained in this work. This is evident from the increases in mean values, first quartile values, lower whisker values, and outlier values.

Table 17 Comparison of mean square error values for the model defined in this work and that by Van Ingen et al. [30]

	Training Data			Validation Data		
	Van Ingen	*This work*		*Van Ingen*	*This work*	
Model	**MSE**	**MSE**	**Difference** [%]	**MSE**	**MSE**	**Difference** [%]
C_L	5.23×10^{-3}	3.55×10^{-3}	−32	4.09×10^{-3}	3.38×10^{-3}	−17
C_D	2.35×10^{-4}	1.68×10^{-4}	−29	1.90×10^{-4}	1.75×10^{-4}	−8
C_X	4.13×10^{-4}	1.20×10^{-4}	−71	1.98×10^{-4}	1.53×10^{-4}	−23
C_Z	5.04×10^{-3}	3.60×10^{-3}	−29	4.07×10^{-3}	3.38×10^{-3}	−17
C_m	1.96×10^{-4}	1.43×10^{-4}	−27	2.52×10^{-4}	1.86×10^{-4}	−26

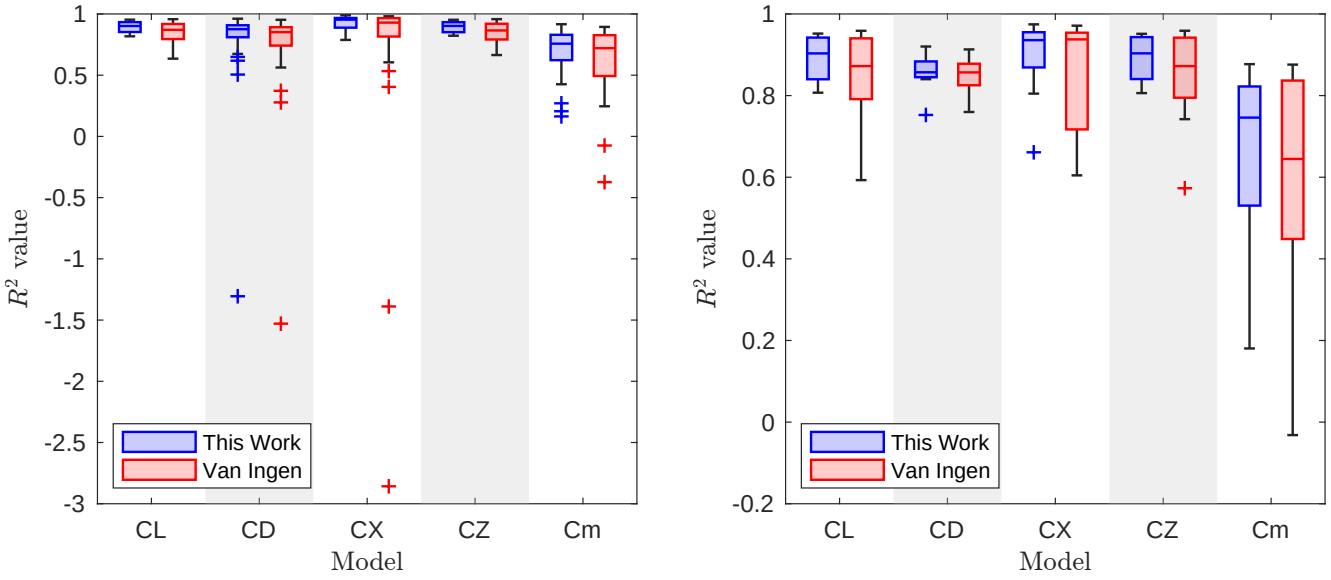

(a) Training data **(b) Validation data**

Fig. 12 Boxplots of the R^2 values of each model. R^2 values are calculated for each maneuver.

Figure 13 shows a comparison of the previous and new models for three selected flight maneuvers of the validation set. These were chosen based on the average R^2 value for the different submodels. The model performed worst for maneuver 46, average performance was found for maneuver 16, and the best performance on maneuver 7. The plots show that, in general, the prediction made by the new model is closer to the measured value.

5 Discussion

5.1 Implications of Separable Nonlinear Least Squares

SNLS is introduced in this paper as an alternative nonlinear parameter estimation technique. Its goal is to overcome three main limitations in prior methods: long runtime, lack of a parameter correlation metric, and suboptimal linear parameter results. The first limitation has been largely eliminated, with runtime reduced from hours to seconds. The second limitation was removed with the introduction of the covariance matrix in Eq. (19). The correlation metric can be derived from the covariance matrix. The third limitation was previously solved by running OLS after the nonlinear parameter estimation. However, this gave inconsistent results between nonlinear and linear parameter estimation methods. SNLS embeds

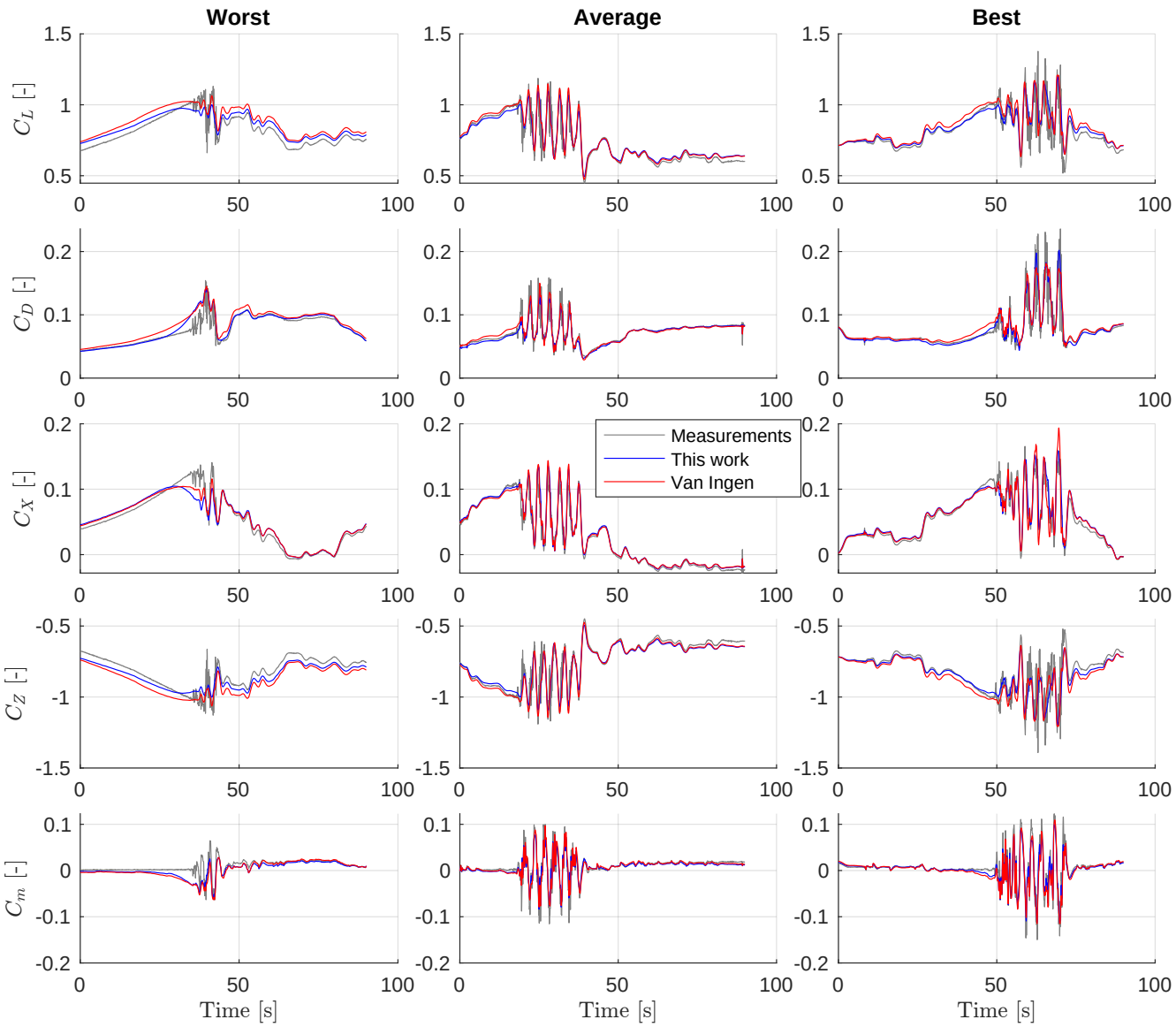

Fig. 13 Performance of the new longitudinal stall model compared with Van Ingen et al. [30] for selected maneuvers. Left shows maneuver 46, the middle shows maneuver 16, and the right shows maneuver 7.

OLS into it for the linear parameters, implying that the parameter estimates are the best linear unbiased estimators of the true parameter values.

The use of SNLS has enabled rapid iteration of model structures, which can be expanded even more in the future. For the separation states and lift coefficient, 15 different nonlinear parameter estimations have been performed. In the past, this was infeasible. The low runtime enables more comprehensive studies to be performed in the future. On top of the runtime improvement, the SNLS method also converges to better parameter values. In Section 4.1, the model of Van Ingen et al. [30] was re-identified and lower MSE values were found on the same maneuvers. The same was found when retaining the same model structure on the new data set created for this paper. Moreover, the results prove more consistent, showing higher averages and smaller spreads in R^2 values.

The potential of the SNLS method is clear, however, work remains in extending the method to lateral flight dynamics. Additionally, the method should be integrated with better model structure selection methods, such as genetic algorithms or exhaustive methods. The use of SNLS has also opened up the option to work with larger data sets. Future work should use this to create composite data sets with stall

and non-stall data. Integrating stall models with nominal models has been a longstanding challenge and this is seen as a potential avenue for closing that gap.

5.2 Stall Model

A new longitudinal stall model for the Cessna Citation II has been presented in this paper. The new model reduces the training MSE by around 30% for the lift, drag, and pitch moment coefficients. Furthermore, the validation MSE is decreased by around 20%.

The model has been extended with a second flow separation state. The second state is hypothesized to correspond to the stall strip. However, this cannot be confirmed without specific tests to visualize the flow around the wing. To this effect, it is suggested for subsequent research to perform flight tests with tufts installed on the wing. Assuming the second state models the local effects of the stall strip. Further research should investigate the use of the model for leading edge stalls specifically. The flow separation model used is typically associated with trailing edge stalls.

No unsteady contributions were found for the wing separation state. It is important to note that these results do not imply that unsteady aerodynamic effects are absent on the rest of the wing. Instead, the available data does not provide significant information for the stall regime in these regions. Furthermore, the deep dynamic stall maneuver proved difficult to execute and further research should work on reliable maneuvers in the high angle of attack regime.

The lift model has been extended and now includes two separation states, as well as a pitch rate and elevator deflection term. There remains a large correlation between the bias and Kirchhoff's term. Although reduced, future work should try to reduce it even further. Furthermore, the effect of the elevator deflection is found to be negative. This is counter-intuitive and likely caused by a high correlation between the elevator deflection and the angle of attack. This can be eliminated by including excitations of the elevator at low angles of attack.

The drag model was changed and now includes a quadratic relation to the lift coefficient. It matches the low and high angle of attack extremes more closely compared to the previous model. Most importantly, it avoids negative drag for negative angles of attack. Still, it would be useful to include more data at negative angles of attack to improve knowledge of that regime.

The pitch moment model saw the most major iteration. It now includes a model for the center of pressure and its shift during a stall. The determination of its location is of great interest for aerodynamic modeling, and future research should investigate it in more detail. Next, a new formulation for the elevator control effectiveness is obtained. The model shows a stagnation of the static pitch moment. Further work should specifically look at that high angle of attack regime where this is observed.

For the drag and pitch moment models, a new dependency on the lift coefficient is introduced. The lift model itself contains errors, which means those are propagated to the drag and pitch moment models. Future work should investigate this propagation. More broadly speaking, an estimate of the confidence in the output of the model is desirable. This can be achieved using uncertainty propagation, which is an area that should be investigated in the future.

This work specifically focuses on the longitudinal dynamics of the stall of the Citation. However, the new SNLS methodology introduced will also benefit model identification of lateral dynamics and no blockers are foreseen for the implementation. Further work should combine specific maneuvers for lateral dynamics with the new identification method. Experimentation with model structures can be performed rapidly and may result in more adequate models.

5.3 Stall Simulation

The ultimate goal of this research is to teach pilots how to safely operate an aircraft during a stall. This paper contributes by improving the accuracy of the aerodynamic force and moment models during the stall. However, future work should determine its effectiveness for pilot training.

First, a study should be performed to judge the propagation of the aerodynamic model towards the aircraft states. By simulating the aircraft dynamics with the aerodynamic model the aircraft states can be compared against the measured states. This might reveal deficiencies present in the model. Additionally, it may also be used to determine if the added complexity is worthwhile.

Similarly, pilot-in-the-loop simulations can determine if it is necessary to include model terms. Through the use of just-noticeable-differences experiments, it can also be determined if the parameter variances found in this work are low enough. Otherwise, more data must be gathered.

6 Conclusion

Stall model identification aims to improve upset prevention and recovery training by enabling accurate flight simulation in stall. This paper contributes to this goal by introducing new flight maneuvers for the Cessna Citation II: the dynamic stall and the deep dynamic stall. These maneuvers reduced τ_1 and τ_2 parameter correlation from 0.73 to 0.06, improving model reliability. Furthermore, a new nonlinear parameter estimation technique was developed, called separable nonlinear least squares. This method significantly reduces the computational time for nonlinear parameter estimation. In addition, larger data sets can be processed, ensuring greater consistency and reducing the risk of overfitting to certain maneuvers. In the future, data sets using stall and non-stall data may be considered to bridge the existing gap of transitioning from nominal to stall models. Further methodological improvements can be made by integrating the separable nonlinear least squares method with model structure selection methods. An improved longitudinal stall model is introduced in this paper, where MSE values for the lift, drag and pitch moment coefficients were reduced by 32%, 29%, and 27%, respectively. The new model should be tested in a simulation where aircraft states can be analyzed. Additionally, pilot-in-the-loop tests should be performed to review the pilots' perception of the new model. Further research should extend the developed longitudinal model to the lateral dynamics of the aircraft using the new methodology. In conclusion, multiple advances have been made that contribute to the overarching goal of improving upset prevention and recovery training, paving the way to safer flight.

A Aircraft Reference Frames

In the paper, three reference frames are used. These reference frames define in which direction forces and moments act. The first reference frame is the earth reference frame, as seen in Figure 14. The origin of this frame is in the center of gravity of the aircraft. The XY-plane is tangential to the surface of the earth, with the X-axis pointing north and the Y-axis pointing east. The Z-axis is perpendicular to the XY-plane and points towards the center of the earth.

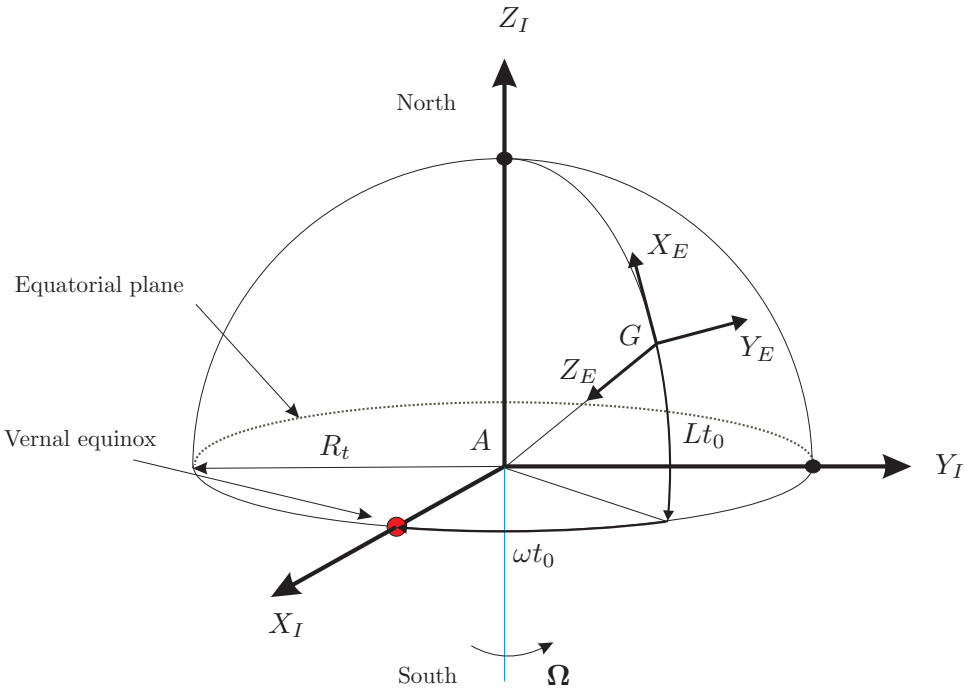

Fig. 14 Earth reference frame, adapted from [47]

The second reference frame, most relevant for flight dynamics modeling, is the body reference frame. This is the frame in which aerodynamic forces and moments are typically expressed. The X-axis is defined through the nose of the aircraft. The Y-axis lies in the horizontal plane and points towards the right wing. Lastly, the Z-axis points downwards and is perpendicular to the X and Y-axis. This reference frame is depicted in Figure 15. The Euler angles can be used to rotate from the earth frame to the body frame. These angles are defined as yaw ψ, pitch θ and roll φ. Using these three angles the rotation matrix $\mathbb{T}_{bE}$ can be constructed:

$$\mathbb{T}_{bE} = \begin{bmatrix} \cos\theta\cos\psi & \cos\theta\sin\psi & -\sin\theta \\ \sin\varphi\sin\theta\cos\psi - \cos\varphi\sin\psi & \sin\varphi\sin\theta\sin\psi + \cos\varphi\cos\psi & \sin\varphi\cos\theta \\ \cos\varphi\sin\theta\cos\psi + \sin\varphi\sin\psi & \cos\varphi\sin\theta\sin\psi - \sin\varphi\cos\psi & \cos\varphi\cos\theta \end{bmatrix} \tag{41}$$

Lastly, the aerodynamic reference frame can be constructed. This frame is aligned with the velocity vector of the incoming undisturbed air. The lift and drag of an aircraft are defined in this reference frame. Its relation to the body frame can be seen in Figure 16. The two angles are the angle of attack α and sideslip β. To rotate from the body frame to the aerodynamic frame rotation matrix $\mathbb{T}_{ab}$ can be used. This rotation matrix is defined as follows:

$$\mathbb{T}_{ab} = \begin{bmatrix} \cos\beta\cos\alpha & \sin\beta & \cos\beta\sin\alpha \\ -\sin\beta\cos\alpha & \cos\beta & -\sin\beta\sin\alpha \\ -\sin\alpha & 0 & \cos\alpha \end{bmatrix} \tag{42}$$

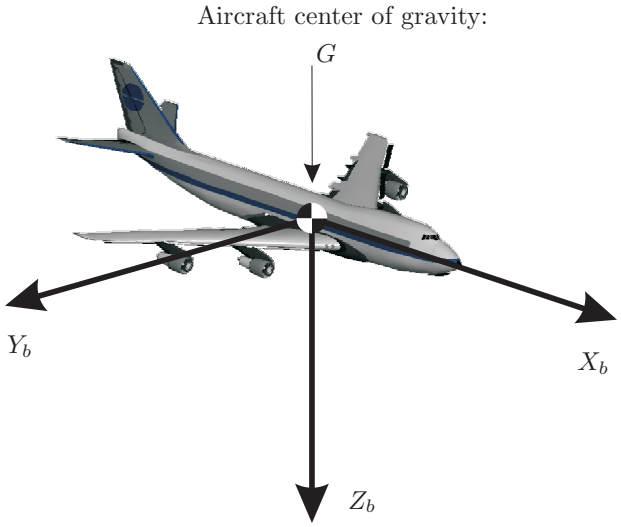

Fig. 15 Body reference frame, adapted from [47]

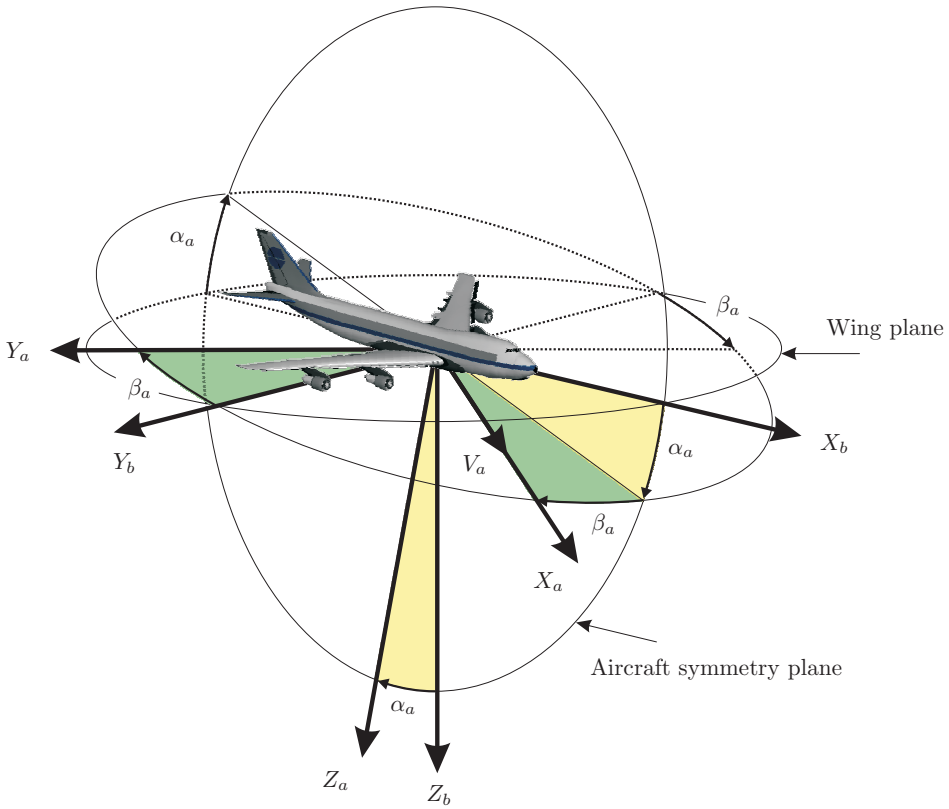

Fig. 16 Aerodynamic reference frame, adapted from [47]

B Model Structures

B.1 Lift Model

The lift models used during exploration are summarized in Table 18.

Table 18 Overview of all experimental lift model structures derived from the base regressors. All models include C_{L_0}.

	$(\alpha - 6°)_+^2$	$K_{L,ss}$	$K_{L,w}$	$\frac{q\bar{c}}{V}$	δ_e
Model CL-I	*	*			
Model CL-II		*			
Model CL-III		*	*		
Model CL-IV		*	*	*	
Model CL-V		*	*		*
Model CL-VI		*	*	*	*

B.2 Drag Model

The drag models used during exploration are summarized in Table 19.

Table 19 Overview of all experimental drag model structures derived from the base regressors. All models include C_{D_0}.

	C_T	$\frac{q\bar{c}}{V}$	δ_e	α	α^2	C_L	C_L^2	$(1 - X_{ss})$	$(1 - X_{ss})$	$K_{D,ss}$	$K_{D,w}$
Model CD-I	*		*	*				*			
Model CD-II	*		*	*				*	*		
Model CD-III	*	*	*					*	*		
Model CD-IV	*	*	*	*				*	*		
Model CD-V	*	*	*		*			*	*		
Model CD-VI	*	*	*	*	*			*	*		
Model CD-VII	*	*	*			*		*	*		
Model CD-VIII	*	*	*				*	*	*		
Model CD-IX	*	*	*			*	*	*	*		
Model CD-X	*	*	*			*					
Model CD-XI	*	*	*				*				
Model CD-XII	*	*	*			*	*				
Model CD-XIII	*	*	*							*	*
Model CD-XIV	*	*	*					*	*	*	*

B.3 Pitch Model

The first model structure for the pitch model is derived from Van Ingen et al. [30].

$$\textbf{Model Cm-I}: \quad C_m = C_{m_0} + C_{m_\alpha}\alpha + C_{m_{X\delta_e}} \max(1/2, X)\delta_e + C_{m_{C_T}} C_T \tag{43}$$

The other model structures are summarized in Table 20. They are supplemented with training MSE on the pitch moment coefficient as not each model is mentioned separately in the main body. Furthermore, the percentage difference from the model by Van Ingen et al. [30] is presented.

Table 20 Overview of all pitch model structures derived from the base regressors. Differences are measured against the pitch model of Van Ingen et al. [30].

	K_0	K_1	$K_2^{1/2}$	K_2^1	K_2^2	K_S	$(1-X)$	$X\delta_e$	C_m MSE	**Difference** [%]
Model Cm-II	*								3.86×10^{-4}	96.7
Model Cm-III		*							3.39×10^{-4}	72.6
Model Cm-IV	*	*							1.53×10^{-4}	−22.2
Model Cm-V	*		*						2.17×10^{-4}	10.8
Model Cm-VI		*	*						3.33×10^{-4}	69.9
Model Cm-VII	*	*	*						1.51×10^{-4}	−22.8
Model Cm-VIII	*			*					2.50×10^{-4}	27.6
Model Cm-IX		*		*					3.32×10^{-4}	69.4
Model Cm-X	*	*		*					1.51×10^{-4}	−23.0
Model Cm-XI	*				*				2.49×10^{-4}	26.3
Model Cm-XII		*			*				3.30×10^{-4}	68.2
Model Cm-XIII	*	*			*				1.49×10^{-4}	−24.1
Model Cm-XIV						*			4.62×10^{-4}	135.3
Model Cm-XV	*					*			2.52×10^{-4}	28.4
Model Cm-XVI							*		3.45×10^{-4}	75.8
Model Cm-XVII	*						*		1.62×10^{-4}	−17.4
Model Cm-XVIII		*					*		3.30×10^{-4}	68.4
Model Cm-XIX	*	*					*		1.47×10^{-4}	−24.9
Model Cm-XX	*		*				*		1.62×10^{-4}	−17.6
Model Cm-XXI		*	*				*		3.18×10^{-4}	62.0
Model Cm-XXII	*	*	*				*		1.41×10^{-4}	−27.9
Model Cm-XXIII	*			*			*		1.61×10^{-4}	−17.9
Model Cm-XXIV		*		*			*		3.17×10^{-4}	61.7
Model Cm-XXV	*	*		*			*		1.39×10^{-4}	−29.1
Model Cm-XXVI	*				*		*		1.57×10^{-4}	−20.2
Model Cm-XXVII		*			*		*		3.18×10^{-4}	61.9
Model Cm-XXVIII	*	*			*		*		1.40×10^{-4}	−28.5
Model Cm-XXIX						*	*		1.80×10^{-4}	−8.3
Model Cm-XXX	*					*	*		1.62×10^{-4}	−17.6
Model Cm-XXXI	*							*	1.68×10^{-4}	−14.5
Model Cm-XXXII		*						*	3.06×10^{-4}	56.0
Model Cm-XXXIII	*	*						*	1.42×10^{-4}	−27.8
Model Cm-XXXIV	*		*					*	1.46×10^{-4}	−25.8
Model Cm-XXXV		*	*					*	3.06×10^{-4}	55.8

Continues on the next page

Table 20 Overview of all pitch model structures derived from the base regressors. Differences are measured against the pitch model of Van Ingen et al. [30]. (continued)

	K_0	K_1	$K_2^{1/2}$	K_2^1	K_2^2	*Singh*	$(1-X)$	$X\delta_e$	C_m MSE	**Difference** [%]
Model Cm-XXXVI	*	*	*					*	1.40×10^{-4}	−28.7
Model Cm-XXXVII	*			*				*	1.57×10^{-4}	−20.2
Model Cm-XXXVIII		*		*				*	3.04×10^{-4}	55.1
Model Cm-XXXIX	*	*		*				*	1.41×10^{-4}	−27.9
Model Cm-XL	*				*			*	1.63×10^{-4}	−16.9
Model Cm-XLI		*			*			*	2.98×10^{-4}	51.9
Model Cm-XLII	*	*			*			*	1.41×10^{-4}	−28.3
Model Cm-XLIII						*		*	2.08×10^{-4}	5.8
Model Cm-XLIV	*					*		*	1.52×10^{-4}	−22.7
Model Cm-XLV							*	*	3.27×10^{-4}	66.5
Model Cm-XLVI	*						*	*	1.45×10^{-4}	−26.1
Model Cm-XLVII		*					*	*	2.85×10^{-4}	45.1
Model Cm-XLVIII	*	*					*	*	1.39×10^{-4}	−29.1
Model Cm-XLIX	*		*				*	*	1.42×10^{-4}	−27.7
Model Cm-L		*	*				*	*	2.84×10^{-4}	45.0
Model Cm-LI	*	*	*				*	*	1.37×10^{-4}	−30.1
Model Cm-LII	*			*			*	*	1.44×10^{-4}	−26.4
Model Cm-LIII		*		*			*	*	2.83×10^{-4}	44.5
Model Cm-LIV	*	*		*			*	*	1.37×10^{-4}	−30.2
Model Cm-LV	*				*		*	*	1.44×10^{-4}	−26.6
Model Cm-LVI		*			*		*	*	2.81×10^{-4}	43.4
Model Cm-LVII	*	*			*		*	*	1.37×10^{-4}	−30.4
Model Cm-LVIII						*	*	*	1.64×10^{-4}	−16.2
Model Cm-LIX	*					*	*	*	1.43×10^{-4}	−27.3

Acknowledgments

The author wishes to thank the test pilots, aircraft technicians, academic staff, and other members of the stall task force for their help during the research project.

Declaration of Use of Artificial Intelligence

Artificial intelligence was not used in the work presented.

References

[1] Mike A. Bromfield and Steven J. Landry. Loss of Control In Flight – time to re-define? In *AIAA Aviation 2019 Forum*, Dallas, Texas, 6 2019. AIAA. ISBN 978-1-62410-589-0. doi: 10.2514/6.2019-3612.

[2] A Statistical Analysis of Commercial Aviation Accidents 1958-2023. Technical report, Airbus, SAS, X00D17008863, 2024.

[3] Statistical Summary of Commercial Jet Airplane Accidents. Technical report, Boeing, Co, 326909, 2023.

[4] Loss of Control In-Flight Accident Analysis Report. Technical report, International Air Transport Association, 2019.

[5] Christine M. Belcastro, John Foster, Richard L. Newman, Loren Groff, Dennis A. Crider, and David H. Klyde. Preliminary Analysis of Aircraft Loss of Control Accidents: Worst Case Precursor Combinations and Temporal Sequencing. In *AIAA Guidance, Navigation, and Control Conference*, National Harbor, Maryland, 1 2014. AIAA. ISBN 978-1-62410-317-9. doi: 10.2514/6.2014-0612.

[6] Steven R Jacobson. Aircraft Loss of Control Causal Factors and Mitigation Challenges. In *AIAA Guidance, Navigation, and Control Conference*, Toronto, Ontario, Canada, 8 2010. AIAA. doi: 10.2514/6.2010-8007.

[7] A. A. Lambregts, G. Nesemeier, J. E. Wilborn, and R. L. Newman. Airplane Upsets: Old Problem, New Issues. In *AIAA Modeling and Simulation Technologies Conference and Exhibit*, Honolulu, Hawaii, 8 2008. AIAA. ISBN 9781563479458. doi: 10.2514/6.2008-6867.

[8] Dennis Crider. Accident Lessons for Stall Upset Recovery Training. In *AIAA Guidance, Navigation, and Control Conference*, Toronto, Ontario, Canada, 8 2010. AIAA. ISBN 978-1-60086-962-4. doi: 10.2514/6.2010-8003.

[9] Sunjoo Advani and Joris Field. Upset Prevention and Recovery Training in Flight Simulators. In *AIAA Modeling and Simulation Technologies Conference*, Portland, Oregon, 8 2011. AIAA. ISBN 978-1-62410-154-0. doi: 10.2514/6.2011-6698.

[10] Manual on Aeroplane Upset Prevention and Recovery Training. Technical report, International Civil Aviation Organization, Doc 10011 AN/506, 2014.

[11] Stall Prevention and Recovery Training. Technical report, Federal Aviation Administration, AC 120-109A, 2017.

[12] Annex I to ED Decision 2019/005/R. Technical report, European Union Aviation Safety Agency, 2019.

[13] Sunjoo K. Advani, Jeffery A. Schroeder, and Bryan Burks. Global Implementation of Upset Prevention & Recovery Training. In *AIAA Modeling and Simulation Technologies Conference*, San Diego, California, USA, 1 2016. AIAA. ISBN 978-1-62410-387-2. doi: 10.2514/6.2016-1430.

[14] N. B. Abramov, M. G. Goman, A. N. Khrabrov, and B. I. Soemarwoto. Aerodynamic Modeling for Poststall Flight Simulation of a Transport Airplane. *Journal of Aircraft*, 56(4):1427–1440, 7 2019. ISSN 1533-3868. doi: 10.2514/1.C034790.

[15] D. Fischenberg. Identification of an unsteady aerodynamic stall model from flight test data. In *20th Atmospheric Flight Mechanics Conference*, pages 138–146, Baltimore, MD, 8 1995. AIAA. ISBN 9780000000002. doi: 10.2514/6.1995-3438.

[16] J. Singh and R. Jategaonkar. Flight determination of configurational effects on aircraft stall behavior. In *21st Atmospheric Flight Mechanics Conference*, pages 657–665, San Diego, CA, 7 1996. AIAA. doi: 10.2514/6.1996-3441.

[17] J. Singh and R. V. Jategaonkar. Identification of lateral-directional behavior in stall from flight data. *Journal of Aircraft*, 33(3):627–630, 5 1996. ISSN 0021-8669. doi: 10.2514/3.46993.

[18] D Fischenberg and R V Jategaonkar. Identification of Aircraft Stall Behavior from Flight Test Data. In *RTO Meeting Proceedings 11, System Identification for Integrated Aircraft Development and Flight Testing*, pages 17(1)–17(8), Madrid, Spain, 1998. NATO, Research and Technology Organization. doi: 10.14339/RTO-MP-011.

[19] Eugene A. Morelli, Kevin Cunningham, and Melissa A. Hill. Global Aerodynamic Modeling for Stall/Upset Recovery Training Using Efficient Piloted Flight Test Techniques. In *AIAA Modeling and Simulation Technologies (MST) Conference*, Boston, MA, 8 2013. AIAA. doi: 10.2514/6.2013-4976.

[20] Joaquim N. Dias. Nonlinear Lifting-Line Algorithm for Unsteady and Post-stall Conditions. In *34th AIAA Applied Aerodynamics Conference*, Washington, D.C., 6 2016. AIAA. ISBN 978-1-62410-437-4. doi: 10.2514/6.2016-4164.

[21] Joaquim N. Dias. Stall Model Identification Using Flight Path Reconstruction of Multiple Maneuvers. In *AIAA Aviation 2023 Forum*, San Diego, CA, 6 2023. AIAA. ISBN 978-1-62410-704-7. doi: 10.2514/6.2023-3781.

[22] L J Van Horssen. Aerodynamic Stall Modeling for the Cessna Citation II. Delft, the Netherlands, 2016. M.Sc. Thesis, Control & Operations Department, Faculty of Aerospace Engineering, Delft University of Technology. URL `http://repository.tudelft.nl/`.

[23] Joost Van Ingen. Dynamic Stall Modeling for the Cessna Citation II. Delft, the Netherlands, 2017. M.Sc. Thesis, Control & Operations Department, Faculty of Aerospace Engineering, Delft University of Technology. URL `http://repository.tudelft.nl/`.

[24] Sven Marschalk. Stall Buffet Modeling using Swept Wing Flight Test Data. Delft, the Netherlands, 2019. M.Sc. Thesis, Control & Operations Department, Faculty of Aerospace Engineering, Delft University of Technology. URL `http://repository.tudelft.nl/`.

[25] Peter C Luteijn. Towards a Stall Model for the Fokker 100. Delft, the Netherlands, 2020. M.Sc. Thesis, Control & Operations Department, Faculty of Aerospace Engineering, Delft University of Technology. URL `http://repository.tudelft.nl/`.

[26] E H P De Meester. Towards an Asymmetric Stall Model for the Fokker 100. Delft, the Netherlands, 2021. M.Sc. Thesis, Control & Operations Department, Faculty of Aerospace Engineering, Delft University of Technology. URL `http://repository.tudelft.nl/`.

[27] A Delfosse. Asymmetric Stall and Control Effectiveness Reduction Modeling for the Cessna Citation II. Delft, the Netherlands, 2021. M.Sc. Thesis, Control & Operations Department, Faculty of Aerospace Engineering, Delft University of Technology. URL `http://repository.tudelft.nl/`.

[28] P A R Brill. Improving Stall Model Accuracy through Optimal Data Slicing by Analyzing Kirch-hoff Stall Parameter Estimate Behaviour. Delft, the Netherlands, 2023. M.Sc. Thesis, Control & Operations Department, Faculty of Aerospace Engineering, Delft University of Technology. URL `http://repository.tudelft.nl/`.

[29] D De Fuijk. Asymmetric Cessna Citation II Stall Model Identification using a Roll Moment-based Kirchhoff Method. Delft, the Netherlands, 2023. M.Sc. Thesis, Control & Operations Department, Faculty of Aerospace Engineering, Delft University of Technology. URL `http://repository.tudelft.nl/`.

[30] Joost B. Van Ingen, Coen C. de Visser, and Daan M. Pool. Stall Model Identification of a Cessna Citation II from Flight Test Data Using Orthogonal Model Structure Selection. In *AIAA Scitech 2021 Forum*. AIAA, 2021. ISBN 9781624106095. doi: 10.2514/6.2021-1725.

[31] G H Golub and V Pereyra. The Differentiation of Pseudo-Inverses and Nonlinear Least Squares Problems Whose Variables Separate. *SIAM Journal on Numerical Analysis*, 10(2):413–432, 4 1973. doi: 10.1137/0710036.

[32] Gene Golub and Victor Pereyra. Separable nonlinear least squares: the variable projection method and its applications. *Inverse Problems*, 19(2):R1–R26, 2 2003. doi: 10.1088/0266-5611/19/2/201.

[33] C C De Visser. *Global Nonlinear Model Identification with Multivariate Splines*. PhD thesis, Delft University of Technology, Delft, the Netherlands, July, 2011.

[34] M. Goman and A. Khrabrov. State-space representation of aerodynamic characteristics of an aircraft at high angles of attack. In *Astrodynamics Conference*. AIAA, 8 1992. doi: 10.2514/6.1992-4651.

[35] J. G. Leishman and T. S. Beddoes. A Semi-Empirical Model for Dynamic Stall. *Journal of the American Helicopter Society*, 34(3):3–17, 7 1989. ISSN 2161-6027. doi: 10.4050/JAHS.34.3.3.

[36] Khiem Van Truong. Modeling Longitudinal Unsteady Aerodynamics of a Wing-Tail Transport Aircraft based on a Dynamic Stall Model. 2 2018.

[37] L C Woods. *The theory of subsonic plane flow*. Cambridge University Press, Cambridge, England, 2011. ISBN 9780521283199.

[38] John D. Anderson. *Fundamentals of Aerodynamics*. McGraw-Hill Education, New York, NY, 6 edition, 2017.

[39] S Marschalk, P C Luteijn, D van Os, D M Pool, and C C de Visser. Stall buffet modeling using swept wing flight test data. In *AIAA Scitech 2021 Forum*, VIRTUAL EVENT, 1 2021. AIAA. ISBN 978-162410609-5 (ISBN). doi: 10.2514/6.2021-0286.

[40] Coen C. de Visser and Daan M. Pool. Stalls and Splines: Current Trends in Flight Testing and Aerodynamic Model Identification. *Journal of Aircraft*, 60(5):1480–1502, 9 2023. ISSN 0021-8669. doi: 10.2514/1.c037283.

[41] Joey Alex Herbold. Aircraft Stall Dynamics: Improved Longitudinal Stall Modeling with Seperable Nonlinear Least Squares and Dynamic Stall Maneuvers. Delft, the Netherlands, 2025. M.Sc. Thesis, Control & Operations Department, Faculty of Aerospace Engineering, Delft University of Technology. URL `http://repository.tudelft.nl/`.

[42] Eastman N Jacobs and William C Clay. Characteristics of The NACA 23012 Airfoil from Full-Scale and Variable-Density Tunnels. Technical report, NASA, 1936.

[43] Noboru Endou and Yasunari Shidama. Differentiation in normed spaces. *Formalized Mathematics*, 21(2):95–102, 2013. ISSN 18989934. doi: 10.2478/forma-2013-0011.

[44] Dianne P. O'Leary and Bert W. Rust. Variable projection for nonlinear least squares problems. *Computational Optimization and Applications*, 54(3):579–593, 4 2013. ISSN 09266003. doi: 10.1007/s10589-012-9492-9.

[45] Kaushik Mahata and Torsten Söderström. Large sample properties of separable nonlinear least squares estimators. *IEEE Transactions on Signal Processing*, 52(6):1650–1658, 6 2004. ISSN 1053587X. doi: 10.1109/TSP.2004.827227.

[46] V. Klein and E.A. Morelli. Aircraft System Identification Theory and Practice. Technical report, AIAA, 2006.

[47] J A Mulder, W H J J Van Staveren, J C Van Der Vaart, E De Weerdt, C C De Visser, A C In 't Veld, and E Mooij. Lecture Notes AE3202 Flight Dynamics. Technical report, Delft University of Technology, 2013.